

Variable Friction Cladding Connection for Seismic Mitigation

Yongqiang Gong¹, Liang Cao², Simon Laflamme^{1,3}, James Ricles², Spencer Quiel², Douglas Taylor⁴

Abstract

Cladding systems are conventionally designed to serve an architectural purpose and provide environmental protection for building occupants. Recent research has been conducted to enhance structural resiliency by leveraging cladding systems against man-made and natural hazards. The vast majority of the work includes the use of sacrificial cladding panels and energy dissipating connectors. These passive protection systems, though effective, have typically targeted a single hazard one-at-a-time because of their limited frequency bandwidths. A novel semi-active friction connection has been previously proposed by the authors to leverage the cladding motion for mitigating blast and wind hazards. This semi-active friction device, termed variable friction cladding connection (VFCC), is designed to laterally connect cladding elements to the structural system and dissipate energy via friction. Its variable friction force is generated onto the sliding friction plates upon which a variable normal force is applied via actuated toggles. Because of its semi-active capabilities, the VFCC could be used over wide-band excitation frequencies and is thereby, an ideal candidate for multiple hazard mitigation. The VFCC in its passive in-situ mode has been previously designed to mitigate air-blast effects towards the structure and its semi-active scheme has been applied to wind hazard mitigation. In this paper, a motion-based design (MBD) procedure is developed to apply the VFCC to seismic hazard mitigation, completing its application against multiple hazards. The MBD procedure begins with the quantification of seismic load and performance objectives, and afterwards, dynamic parameters of the cladding connection are selected based on non-dimensional analytical solutions. Simulations are conducted on two example buildings to verify and demonstrate the motion-based design methodology. Results show the semi-actively controlled VFCC is capable of mitigating the seismic vibrations of structures, demonstrating the promise of the semi-active cladding system for field applications.

Keywords: Motion-based design, cladding connection, seismic mitigation, semi-active control, variable friction, high performance control system

¹Department of Civil, Construction, and Environmental Engineering, Iowa State University, Ames, IA 50011, U.S.A

²Department of Civil and Environmental Engineering, Lehigh University, Bethlehem, PA 18015, U.S.A

³Department of Electrical and Computer Engineering, Iowa State University, Ames, IA 50011, U.S.A

⁴Taylor Devices, North Tonawanda, NY 14120, U.S.A

1. Introduction

Motion-based design (MBD) is a design approach in which a structural system is designed to ensure satisfactory dynamic performance under design loads [1]. MBD also includes the design and incorporation of supplemental damping systems when necessary. Over the last decades, numerous passive energy dissipation systems have been deployed in building systems, such as hysteretic [2, 3], friction [4, 5], viscoelastic [6, 7], viscous fluid [8, 9], and tuned mass dampers [10, 11]. Such passive energy dissipation systems are well accepted by the field due to their high mechanical robustness and demonstrated mitigation capabilities [12].

Of interest to this paper are energy dissipation systems that leverage cladding motion to dissipate energy, termed multi-functional cladding systems. In buildings, a typical cladding system transfers both its self-weight and lateral loads due to exterior pressure (wind and blast) or its inertia (seismic) to the structural system. A common multi-functional cladding application is found in blast mitigation, where the cladding itself is designed to dissipate blast loads. Examples include sacrificial cladding panels with double-layer foam cladding [13, 14], tube-core cladding [15, 16], sandwich cladding [17, 18], and metal layer cladding [19, 20]. Others have proposed to dissipate blast through the cladding connection using, for example, rotational friction hinge [21, 22], viscoelastic spider [23], and metallic yielding [24] connections.

Previous studies have also proposed passive cladding connections for wind and seismic application. Goodno and Craig [25] have tested ductile cladding connections with heavyweight cladding panels for seismic vibration mitigation. Baird *et al.* [26] have experimentally investigated the seismic mitigation performance of a U-shape flexural plate connector fabricated by bending mild steel plate. Azad *et al.* [27, 28] have studied damped cladding brackets in curtain wall systems to reduce wind-induced motion. Biondini *et al.* [29] and Ferrara *et al.* [30] have evaluated the performance of bolted friction connectors joining cladding elements for energy dissipation. Maneetes *et al.* [31] have implemented supplementary friction devices in spandrel-type precast concrete cladding systems to provide lateral force resistance. Dal Lago *et al.* [32] have tested steel W-shaped folded plate dissipative connectors in precast concrete cladding systems for seismic mitigation. Vibration mitigation by leveraging the inertia of the cladding weight has also been proposed. Examples can be found in Refs. [33, 34, 35] where double skin facade systems are utilized as multiple tuned mass damper systems.

The vast majority of these surveyed advances are limited to the mitigation of single types of hazards one-at-a-time. This can be attributed to the bandwidth-limited performance of passive systems [36, 37]. A solution to improve the performance of structural system versus a variety of hazard types, termed multi-hazards, is to leverage high performance control systems (HPCSs). HPCSs include active [38, 39, 40], semi-active [41, 42, 43] and hybrid control strategies [44, 45, 46]. These systems are capable of higher performance over a large bandwidth due to their adaptive capabilities, ideal for multi-hazard mitigation [47, 48].

35 The authors have proposed a semi-active variable friction cladding connection (VFCC). The VFCC is
36 engineered to provide a lateral connection between cladding elements to the structural system. The variable
37 friction mechanism consists of sliding friction plates onto which a variable normal force can be applied through
38 an actuated toggle system. Variable friction has been widely studied in structural control with devices
39 leveraging electromechanical- [49, 50], electromagnetic- [51, 52], magnetorheological- [53, 54], hydraulic-
40 [41, 55], and piezoelectric- [56, 57] based actuation. Prior work on the VFCC consisted of prototyping and
41 characterizing the device [58], and developing an MBD methodology for blast [59] and wind [60] mitigation.
42 In this paper, MBD procedures are developed for the mitigation of seismic events based on analytical transfer
43 functions that characterize the dynamic response of a structure-cladding system to ground motion. This
44 paper demonstrates its novelty by aiming at seismic mitigation with the VFCC designed using an MBD
45 methodology.

46 The paper is organized as follows:

- 47 • Section 2 gives the background on the VFCC.
- 48 • Section 3 derives analytical transfer functions for a structure-cladding system necessary in enabling
49 the MBD procedure.
- 50 • Section 4 presents the MBD procedure to conduct cladding connection design.
- 51 • Section 5 verifies and demonstrates the MBD procedure through numerical simulations on two example
52 buildings.

53 **2. Variable Friction Cladding Connection**

54 The VFCC is engineered to transfer lateral loads acting on the cladding elements to the structural
55 system. The device is diagrammed in Fig. 1(a). It consists of two sets of sliding friction plates upon which
56 an adjustable normal force is applied through an actuated toggle system. Blocks are used to prevent the
57 toggles from pushing beyond their vertical alignment. Fig. 1(b) provides a picture of a prototype used in
58 the characterization of its friction mechanism, published previously by the authors [58]. In this prototype,
59 the actuator stroke was emulated using spacers that maintained a constant displacement between toggles,
60 and the VFCC was mounted in an aluminum frame for testing.

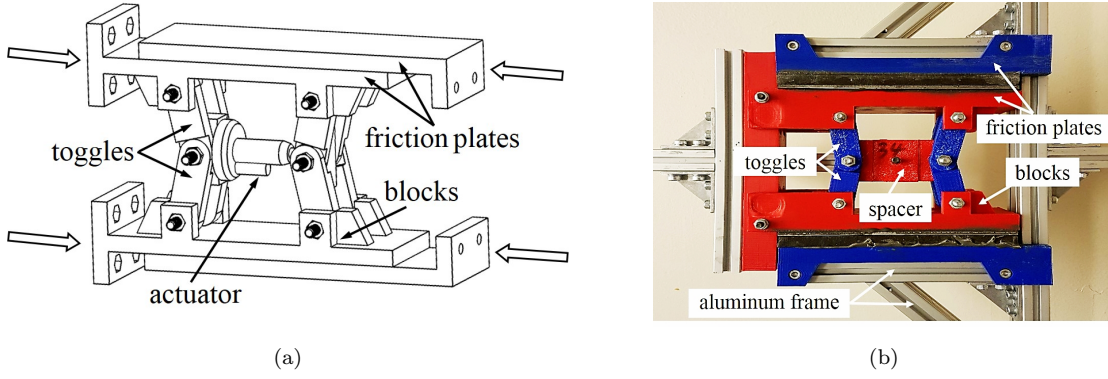


Figure 1: (a) Diagram of the VFCC; and (b) annotated picture of a prototype.

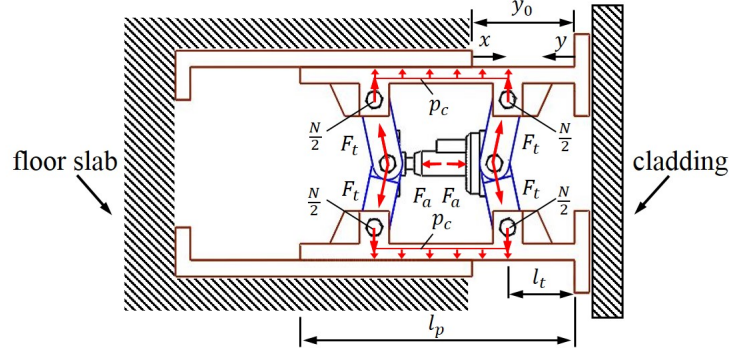


Figure 2: Force diagram for the VFCC installed into a floor slab (top view).

61 Fig. 2 illustrates a possible installation scheme of the VFCC embedded into a floor slab, along with the
 62 associated force diagram. To provide lateral connection, the inner friction plates of the VFCC are extended
 63 outward to attach the cladding panel. An actuation force F_a generates axial forces F_t on the toggles, which
 64 generates a distributed pressure p_c onto the friction plates:

$$p_c = \frac{F}{A_{c,\max}} \quad (1)$$

65 where F is the generated normal force and $A_{c,\max} = b_p(l_p - 2l_t)$ is the maximum contact area of the friction
 66 plates of width b_p (not shown in Fig. 2) and length l_p with distance l_t extending beyond the toggle location.
 67 The generated Coulomb friction force F_c is taken as proportional to the effective contact area A_c between
 68 the friction plates under pressure p_c with

$$F_c = \mu_c F \frac{A_c}{A_{c,\max}} = \begin{cases} 2\mu_c F & \text{if } 0 \leq y < l_t \\ 2\mu_c F \frac{l_p - l_t - y}{l_p - 2l_t} & \text{if } l_t \leq y \leq l_p - l_t \\ 0 & \text{if } l_p - l_t < y \leq l_p \end{cases} \quad (2)$$

69 where the effective contact area A_c varies with their relative displacement y , and μ_c is the friction coefficient.

70 From prior work conducted on the VFCC in a laboratory environment [58], a LuGre friction model can
 71 be used to characterize the dynamic friction force F_f

$$F_f(x) = \sigma_0 \zeta + \sigma_1 \dot{\zeta} + \sigma_2 \dot{x} \quad (3)$$

72 with

$$\dot{\zeta} = \dot{x} - \sigma_0 \frac{|\dot{x}|}{g(\dot{x})} \zeta \quad (4)$$

$$g(\dot{x}) = F_c(x) + [F_s(x) - F_c(x)] e^{-(\dot{x}/\dot{x}_m)^2} \quad (5)$$

73 where σ_0 represents the stiffness of the bristles, σ_1 microdamping, σ_2 viscous friction, ζ an evolutionary
 74 variable, x the sliding displacement of the inner friction plates and taken as $x = y_0 - y$, \dot{x} the sliding velocity,
 75 $g(\dot{x})$ a governing function of the Stribeck effect, \dot{x}_m the constant Stribeck velocity, and $F_s(x)$ and $F_c(x)$ the
 76 magnitude of the Stribeck effect and the Coulomb friction force, respectively.

77 The characterization process was conducted by subjecting the VFCC to various harmonic excitations
 78 under different actuation capacities (%). Fig. 3 shows typical force-displacement and force-velocity loops of
 79 a 1 kN capacity device under various utilization levels (%) using the parameterized LuGre (Table 1) model
 80 under a configuration of $l_t \leq y \leq l_p - l_t$. Parameters σ_0 and F_s are modeled as proportional functions of the
 81 Coulomb friction force F_c

$$\sigma_0 = C_\sigma F_{c0} + \sigma_0|_{F_{c0}=0} \quad (6)$$

$$F_s = C_s F_c = C_s F_{c0} \frac{l_p - l_t - y_0 + x}{l_p - l_t - y_0} \quad (7)$$

82 where $C_s > 1$ and C_σ are constants and F_{c0} represents the initial Coulomb friction force at $x = 0$.

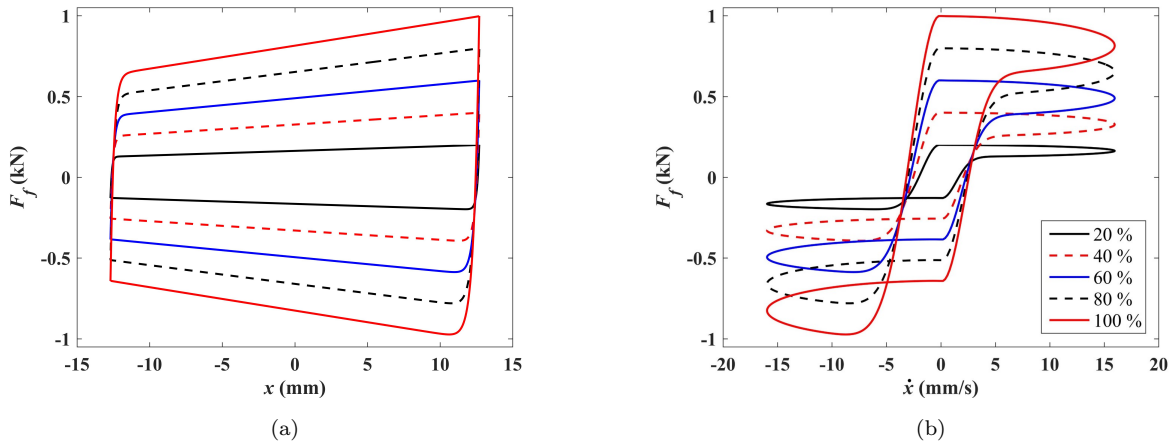


Figure 3: Dynamics of the VFCC under a harmonic excitation of amplitude 13 mm at 0.2 Hz and various levels of actuation capacity: (a) force-displacement loop; and (b) force-velocity loop.

Table 1: Parameters of the VFCC prototype [58].

parameter	units	value
l_p	mm	165
b_p	mm	60
l_t	mm	45
C_s	—	1.052
C_σ	mm ⁻¹	2.185
$\sigma_0 _{F_{c0}=0}$	kN·mm ⁻¹	1.147
σ_1	N·s·mm ⁻¹	0.200
σ_2	N·s·mm ⁻¹	0.200

83 3. Analytical Transfer Functions

84 In this section, two analytical transfer functions of a structure-cladding system are derived as part of the
 85 MBD approach. The equations of motion are first presented, followed by the derivation of non-dimensional
 86 transfer functions.

87 3.1. Equations of motion

88 Consider an n -story lumped-mass shear structure equipped with a cladding system connected through
 89 VFCCs illustrated in Fig. 4. A cladding panel is designed to span between two floors and is represented by a
 90 uniform rigid bar. The lateral cladding connection is represented by stiffness element k_c , a viscous damping
 91 element c_{c0} , and a variable friction element F_f (Eq. (3)), while the gravitational support is considered as
 92 decoupled and provided by conventional gravity connections. In order to facilitate the derivation of analytical
 93 solutions, the equations of motion for the structure-cladding system are built upon the assumption that the
 94 variable friction element F_f is approximated by an equivalent linear viscous damping representation c_v . The
 95 quality of this assumption will be verified in Section 5.1. The resulting equivalent viscous damping element
 96 c_c for the connection is written

$$c_c = c_{c0} + \frac{4F_f}{\pi\Omega\hat{x}} \quad (8)$$

97 where Ω is the excitation frequency and \hat{x} is the amplitude of structure-cladding displacement under a
 98 harmonic load. The equations of motion of the n -story structure-cladding system with equivalent viscous
 99 damping under a harmonic seismic load are written

$$\mathbf{M}_s \ddot{\mathbf{x}}_s + \mathbf{C}_s \dot{\mathbf{x}}_s + \mathbf{K}_s \mathbf{x}_s = -\mathbf{M}_s \mathbf{E}_s \ddot{x}_g + \mathbf{E} \mathbf{C}_c \dot{\mathbf{x}}_c + \mathbf{E} \mathbf{K}_c \mathbf{x}_c \quad (9)$$

$$\mathbf{M}_c \ddot{\mathbf{x}}_c + \mathbf{C}_c \dot{\mathbf{x}}_c + \mathbf{K}_c \mathbf{x}_c = -\mathbf{M}_c \mathbf{E}_c \ddot{x}_g - \mathbf{M}_c \mathbf{E}^T \ddot{\mathbf{x}}_s \quad (10)$$

100 where $\mathbf{x}_s \in \mathbb{R}^{n \times 1}$ and $\mathbf{x}_c \in \mathbb{R}^{2n \times 1}$ are the displacement vectors of the primary structure and of the cladding
101 relative to the structure, respectively, $\mathbf{E} \in \mathbb{R}^{n \times 2n}$ is the cladding location matrix, \ddot{x}_g is the ground acceleration
102 excitation, $\mathbf{E}_s \in \mathbb{R}^{n \times 1}$ and $\mathbf{E}_c \in \mathbb{R}^{2n \times 1}$ are the location matrices of the excitation input on the primary
103 structure and cladding elements, respectively, $\mathbf{M}_c \in \mathbb{R}^{2n \times 2n}$, $\mathbf{C}_c \in \mathbb{R}^{2n \times 2n}$, $\mathbf{K}_c \in \mathbb{R}^{2n \times 2n}$ are the mass,
104 damping, and stiffness matrices of the cladding elements, respectively, and $\mathbf{M}_s \in \mathbb{R}^{n \times n}$, $\mathbf{C}_s \in \mathbb{R}^{n \times n}$, $\mathbf{K}_s \in$
105 $\mathbb{R}^{n \times n}$ are the mass, damping, and stiffness matrices of the primary structure, respectively.

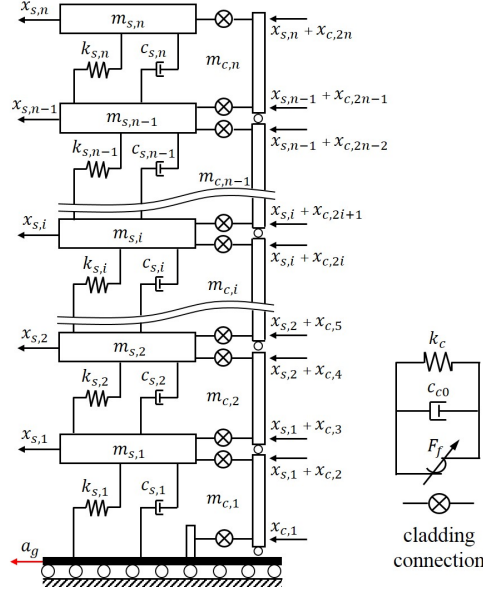


Figure 4: Schematic representation of an n -story structure equipped with a cladding system and VFCCs.

106 For simplicity of the design process and field implementation, the cladding mass m_c , the lateral connection
107 stiffness k_c , and the equivalent connection damping c_c , are assumed to be identical at each floor. The
108 dynamics of the i^{th} cladding element is studied using a two degrees-of-freedom (DOFs) representation where
109 the cladding element is connected to floors i and $i - 1$ (Fig.5(a)). Its associated equations of motion is

$$\mathbf{m}_c \ddot{\mathbf{x}}_{c,i} + \mathbf{c}_c \dot{\mathbf{x}}_{c,i} + \mathbf{k}_c \mathbf{x}_{c,i} = -\mathbf{m}_c \mathbf{e}_c \ddot{x}_g - \mathbf{m}_c \ddot{\mathbf{x}}_{s,i} \quad (11)$$

110 where $\mathbf{x}_{s,i} = [x_{s,i-1} \quad x_{s,i}]^T$ and $\mathbf{x}_{c,i} = [x_{c,2i-1} \quad x_{c,2i}]^T$ are the displacement vectors of the structural floors
111 and of the i^{th} cladding element relative to the primary structure, respectively, and $\mathbf{e}_c = [1 \quad 1]^T$ is the
112 excitation location vector. The displacement vector $\mathbf{x}_{c,i}$ is expressed in terms of the modal vectors Φ_{cr} and
113 modal coordinates $q_{cr,i}$ ($r = 1, 2$), and is assumed to be governed by the first mode

$$\mathbf{x}_{c,i} \approx \Phi_{c1} q_{c1,i} \quad (12)$$

114 where $q_{c1,i}$ is the modal coordinate of the first mode and $\Phi_{c1} = [\phi_{c,11} \quad \phi_{c,12}]^T = [1 \quad 1]^T$, obtained by
115 solving the algebraic equation $[\mathbf{k}_c - \omega_c^2 \mathbf{m}_c] \Phi_{c1} = \mathbf{0}$ [61].

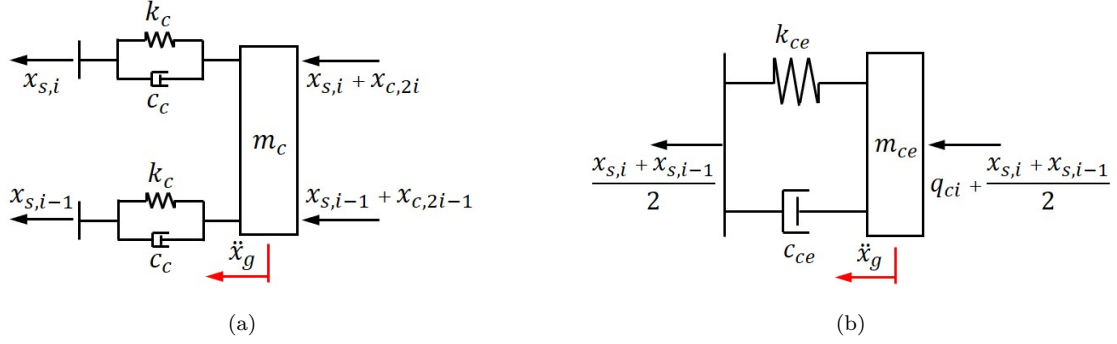


Figure 5: Representation of the i^{th} cladding element connected to adjacent floors: (a) two DOFs; and (b) SDOF representations.

116 Pre-multiplying Eq. 11 by Φ_{c1}^T and substituting $\mathbf{x}_{c,i}$ from Eq. 12 gives an expression for the governing
 117 dynamics of the cladding element, which can be represented by a single DOF (SDOF) system (Fig. 5(b))

$$m_{ce}\ddot{q}_{c1,i} + c_{ce}\dot{q}_{c1,i} + k_{ce}q_{c1,i} = -m_{ce}\ddot{x}_g - m_{ce}\frac{\ddot{x}_{s,i-1} + \ddot{x}_{s,i}}{2} \quad (13)$$

118 with the equivalent cladding mass m_{ce} , damping c_{ce} , and stiffness k_{ce}

$$m_{ce} = \Phi_{c1}^T \mathbf{m}_c \Phi_{c1} = m_c \quad ; \quad c_{ce} = \Phi_{c1}^T \mathbf{c}_c \Phi_{c1} = 2c_c \quad ; \quad k_{ce} = \Phi_{c1}^T \mathbf{k}_c \Phi_{c1} = 2k_c$$

119 where the nodal displacement $q_{c1,i} \approx x_{c,2i-1} \approx x_{c,2i}$.

120 Similarly, the displacement vector of the primary structure \mathbf{x}_s is expressed in terms of the modal vectors
 121 Φ_{si} and coordinates q_{si} ($i = 1, 2, \dots, n$), and the first modal shape is assumed to govern its dynamics

$$\mathbf{x}_s = \sum_{i=1}^n \Phi_{si} q_{si} \approx \Phi_{s1} q_{s1} \quad (14)$$

122 where the first modal shape $\Phi_{s1} = [\phi_{s,11} \quad \phi_{s,12} \quad \dots \quad \phi_{s,1n}]^T$ with $\phi_{s,1n}$ normalized to unity. Pre-
 123 multiplying Eq. 9 by Φ_{s1}^T yields an uncoupled equation for q_{s1} ,

$$m_{se}\ddot{q}_{s1} + c_{se}\dot{q}_{s1} + k_{se}q_{s1} = -\Phi_{s1}^T \mathbf{M}_s \mathbf{E}_s \ddot{x}_g + \Phi_{s1}^T \mathbf{E} \mathbf{C}_c \dot{\mathbf{x}}_c + \Phi_{s1}^T \mathbf{E} \mathbf{K}_c \mathbf{x}_c \quad (15)$$

124 where the displacement of the SDOF structure $q_{s1} \approx x_{s1}$ and its dynamic properties are defined as

$$m_{se} = \Phi_{s1}^T \mathbf{M}_s \Phi_{s1} \quad ; \quad c_{se} = \Phi_{s1}^T \mathbf{C}_s \Phi_{s1} \quad ; \quad k_{se} = \Phi_{s1}^T \mathbf{K}_s \Phi_{s1} \quad (16)$$

125 with the structural damping matrix \mathbf{C}_s taken as linear proportional to the structural stiffness matrix \mathbf{K}_s .

126 The governing equations of the structure-cladding system are subsequently reduced to

$$m_{se}\ddot{q}_{s1} + c_{se}\dot{q}_{s1} + k_{se}q_{s1} = -\sum_{i=1}^n \phi_{s,1i} m_{si} \ddot{x}_g + \sum_{i=1}^n \alpha_i (k_{ce} q_{c1,i} + c_{ce} \dot{q}_{c1,i}) \quad (17)$$

$$m_{ce}\ddot{q}_{c1,i} + c_{ce}\dot{q}_{c1,i} + k_{ce}q_{c1,i} = -m_{ce}\ddot{x}_g - \alpha_i m_{ce} \ddot{q}_{s1} \quad (18)$$

127 where $\alpha_i = \frac{1}{2}(\phi_{s,1i-1} + \phi_{s,1i})$ for $i = 2, \dots, n$ and $\alpha_i = \frac{1}{2}\phi_{s,1i}$ for $i = 1$.

128 *3.2. Transfer functions*

129 To derive mathematically trackable non-dimensional transfer functions, the ground acceleration $\ddot{x}_g(t)$ is
 130 represented by a harmonic excitation $\ddot{x}_g(t) = \hat{x}_g e^{j\Omega t}$, where \hat{x}_g is the amplitude of excitation. Following
 131 the standard derivation for the steady state response of the reduced structure-cladding system [1, 60], the
 132 amplitudes of the responses are written

$$\begin{aligned} \frac{\hat{q}_{s1} e^{j\delta_s}}{\hat{x}_g} &= -\frac{(k_{ce} + jc_{ce}\Omega)\Gamma_1 m_{ce} + (k_{ce} - \Omega^2 m_{ce} + jc_{ce}\Omega) \sum_{i=1}^n \phi_{s,1i} m_{si}}{(k_{se} - m_{se}\Omega^2 + jc_{se}\Omega)(k_{ce} - m_{ce}\Omega^2 + jc_{ce}\Omega) - (k_{ce} + jc_{ce}\Omega)\Gamma_2 m_{ce}\Omega^2} \\ \frac{\hat{q}_{c1,i} e^{j\delta_{ci}}}{\hat{x}_g} &= \frac{-m_{ce} + \alpha_i m_{ce}\Omega^2 \hat{q}_{s1} e^{j\delta_s} / \ddot{x}_{g0}}{k_{ce} - m_{ce}\Omega^2 + jc_{ce}\Omega} \end{aligned} \quad (19)$$

133 where the hat denotes an amplitude, j the imaginary unit, δ the phase angles, $\Gamma_1 = \sum_{i=1}^n \alpha_i$, and $\Gamma_2 = \sum_{i=1}^n \alpha_i^2$
 134 .

135 Defining the mass ratio μ , tuning frequency ratio f , and excitation frequency ratio λ between the cladding
 136 and the structure

$$\mu = \frac{m_{ce}}{m_{se}} \quad ; \quad f = \frac{\omega_c}{\omega_s} \quad ; \quad \text{and} \quad \lambda = \frac{\Omega}{\omega_s} \quad (20)$$

137 with

$$\omega_s = \sqrt{\frac{k_{se}}{m_{se}}} \quad ; \quad \xi_s = \frac{c_{se}}{2m_{se}\omega_s} \quad ; \quad \omega_c = \sqrt{\frac{k_{ce}}{m_{ce}}} \quad ; \quad \text{and} \quad \xi_c = \frac{c_{ce}}{2m_{ce}\omega_c} \quad ;$$

138 gives the non-dimensional transfer functions $H_s(\lambda)$ and $H_{c,i}(\lambda)$ that represent the dynamic amplification of
 139 the displacement of the SDOF structure and of the displacement of the i^{th} cladding relative to its connected
 140 floor, respectively, where

$$H_s(\lambda) = \frac{\hat{q}_{s1} e^{j\delta_s}}{m_{se} \hat{x}_g / k_{se}} = -\frac{\mu\Gamma_1 f^2 + (f^2 - \lambda^2)\Gamma_m + j2\xi_c f \lambda (\mu\Gamma_1 + \Gamma_m)}{(1 - \lambda^2)(f^2 - \lambda^2) - 4\xi_c \xi_s f \lambda^2 - \mu\Gamma_2 f^2 \lambda^2 + j[2\xi_c f \lambda (1 - (1 + \mu\Gamma_2)\lambda^2) + 2\xi_s \lambda (f^2 - \lambda^2)]} \quad (21)$$

$$H_{c,i}(\lambda) = \frac{\hat{q}_{c1,i} e^{j\delta_{ci}}}{m_{se} \hat{x}_g / k_{se}} = \frac{\alpha_i \lambda^2 H_s(\lambda) - 1}{f^2 - \lambda^2 + j2\xi_c f \lambda} \quad (22)$$

141 with $\Gamma_m = \sum_{i=1}^n \phi_{s,1i} m_{si} / m_{se}$.

142 **4. Motion-Based Design Procedure**

143 This section describes the MBD procedure to size the semi-active cladding connection for seismic hazard
 144 mitigation. The design phase starts by assuming a passive damping behavior where the VFCC is approxi-
 145 mated as a linear viscous damping element. Such design strategy is common in designing HPCSs to a target
 146 capacity [37, 62, 63]. Fig. 6 diagrams the MBD procedure. First, the design seismic load is quantified
 147 using a design spectrum compatible power spectral density function (PSDF) $G(\omega)$. Second, the performance

148 objectives are defined, which include the peak inter-story drift ratio Δ_p and the peak structure-cladding
 149 spacing l_c . Other objectives could also be considered, such as peak acceleration. Third, preliminary design
 150 values are obtained for the equivalent stiffness k_{ce} and viscous damping ratio ξ_c , after which the maximum
 151 drift ratio Δ_{\max} and the maximum structure-cladding spacing l_{\max} are computed using non-dimensional an-
 152 alytical solutions R_s and R_c , respectively and compared against the performance metrics. If the performance
 153 is unsatisfactory, the design is iterated by either redesigning connection parameters k_{ce} and ξ_c (option 1) or
 154 updating the allowable structure-cladding spacing l_c (option 2). These design steps are explained in what
 155 follows.

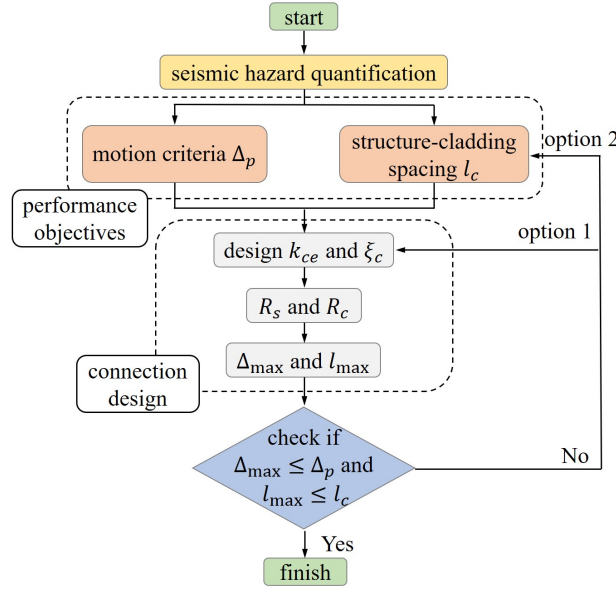


Figure 6: Motion-based design procedure.

156 4.1. Seismic hazard model

157 The seismic acceleration is assumed to be a zero-mean Gaussian stationary process characterized by a
 158 one-sided design spectrum compatible PSDF $G(\omega)$ in the frequency domain [64, 65]. The PSDF $G(\omega)$ will
 159 be integrated with transfer functions to compute the peak structural response in Section 4.3.1. A discrete
 160 design PSDF $G(\omega_N)$ is obtained using the design response spectrum $S_g(\omega_N, \xi)$ with the following equations
 161 [64]

$$G(\omega_N)\omega_N \left(\frac{\pi}{4\xi} - 1 \right) + \int_0^{\omega_N} G(\omega)d\omega = \frac{S_g^2(\omega_N, \xi)}{\eta_N^2} \quad (23)$$

162 with $\omega_N = \omega_1 + (N - 1)\Delta\omega$ the discretized frequency of frequency interval $\Delta\omega$ and excitation lowest fre-
 163 quency bound ω_1 , and where ξ is the damping ratio of a lightly damped SDOF system associated with the
 164 design response spectrum $S_g(\omega_N, \xi)$, and η_N is a critical factor that establishes the equivalence between the

165 $S_g(\omega_N, \xi)$ and $G(\omega_N)$ with probability of exceedance p . A semi-empirical formula is used to compute the
 166 peak factor η_N [66]

$$\eta_N = \sqrt{2 \ln \left\{ 2v_N \left[1 - \exp \left(-u^{1.2} \sqrt{\pi \ln(2v_N)} \right) \right] \right\}} \quad (24)$$

167 with

$$v_N = \frac{T_e}{2\pi} \omega_N (-\ln p)^{-1} \quad (25)$$

168 and

$$u = \sqrt{1 - \frac{1}{1 - \xi^2} \left(1 - \frac{2}{\pi} \tan^{-1} \frac{\xi}{\sqrt{1 - \xi^2}} \right)^2} \quad (26)$$

169 where T_e is the time duration of excitation. Using a discrete summation to approximate the integral in Eq.
 170 23 and rearranging yields an expression of a discrete response spectrum compatible PSDF $G(\omega_N)$ [64, 67]

$$G(\omega_N) = \frac{4\xi}{\omega_N \pi - 4\xi \omega_{N-1}} \left(\frac{S_g^2(\omega_N, \xi)}{\eta_N^2(\omega_N, \xi)} - \Delta\omega \sum_{k=1}^{N-1} G(\omega_k) \right) \quad \omega_N > \omega_1 \quad (27)$$

171 where the approximately obtained PSDF $G(\omega_N)$ is further updated through a match of its associated re-
 172 sponse spectrum $S_{g,\text{new}}(\omega_N, \xi)$ with the target design spectrum $S_g(\omega_N, \xi)$. The associated response spectrum
 173 $S_{g,\text{new}}(\omega_N, \xi)$ is obtained by substituting $G(\omega_N)$ back into Eq. 23, and an updated PSDF $G_{\text{new}}(\omega_N)$ is com-
 174 puted using the following iteration scheme until a conversion error of one ten thousandth is obtained

$$G_{\text{new}}(\omega_N) = G(\omega_N) \left[\frac{S_g(\omega_N, \xi)}{S_{g,\text{new}}(\omega_N, \xi)} \right]^2 \quad (28)$$

175 The target response spectrum $S_g(\omega_N, \xi)$ or $S_g(T_N, \xi)$ for a fundamental period $T_N = 2\pi/\omega_N$, assuming
 176 a damping ratio $\xi = 0.05$, is defined in ASCE 7-10 (2010) [68]

$$S_g(T_N, \xi) = \begin{cases} S_{DS}(0.4 + 0.6T_N/T_0) & 0 \leq T_N < T_0 \\ S_{DS} & T_0 \leq T_N < T_1 \\ S_{D1}/T_N & T_1 \leq T_N < T_L \\ S_{D1}T_L/T_N^2 & T_N \geq T_L \end{cases} \quad (29)$$

where S_{DS} and S_{D1} are the design spectral response acceleration parameters at the short-period $T_0 = 0.2S_{D1}/S_{DS}$ and at 1 s, respectively, $T_1 = S_{D1}/S_{DS}$ and T_L is the long-period transition period (ASCE 7-10 (2010) [68]). A damping modification factor S_{DMF} is introduced to obtain the response spectra $S_g(T_N, \xi_s)$ with structural damping ratio ξ_s , where [69]

$$S_{\text{DMF}} = \frac{S_g(T_N, \xi_s)}{S_g(T_N, \xi)} = \left(\frac{7}{2 + 100\xi_s} \right)^{0.25} \quad (30)$$

177 The duration of the excitation is taken as $T_e = 20$ s, with associated probability $p = 0.5$ and lowest
 178 frequency bound $\omega_1 = 0.5$ rad/s [64].

179 *4.2. Performance objectives*

180 Motion criteria for seismic design are generally associated with structural damage states and often follow
 181 limits on inter-story drifts. The threshold of the maximum inter-story drift varies with structure types. Here,
 182 criteria for typical steel moment-resisting framed structures are used, listed in Table 2 [70, 71]. The perfor-
 183 mance of a steel building equipped with structural control systems can be set to an immediate occupancy
 184 level or a damage-repairable state, with a drift limit range of $0.2\% < \Delta_p < 1.5\%$ [72, 73].

185 The structure-cladding spacing can be accommodated for the ease of manufacture, installation, and
 186 maintenance of the lateral connections. A minimum structure-cladding spacing for a lateral connections l_{\min}
 187 can be as high as 15 cm [74]. The allowable structure-cladding gap l_c for preliminary design is selected such
 188 that $l_c > l_{\min}$.

Table 2: Performance levels and corresponding damage states and drift limits [70, 71].

performance level	damage state	drift ratio (%)
immediate occupancy	none	$\Delta_p < 0.2$
	slight	$0.2 < \Delta_p < 0.5$
	light	$0.5 < \Delta_p < 0.7$
	moderate	$0.7 < \Delta_p < 1.5$
life safety	heavy	$1.5 < \Delta_p < 2.5$
	major	$2.5 < \Delta_p < 5.0$
collapse prevention	collapsed	$\Delta_p > 5.0$

189 *4.3. Connection design*

190 The selection of cladding connection parameters is conducted through an iterative process. It consists of
 191 establishing parameters, computing the peak building responses, and verifying the performance metrics. The
 192 computation of the peak building responses is conducted based on two non-dimensional analytical solutions
 193 R_s and R_c , yielding the maximum inter-story drift Δ_{\max} and the maximum structure-cladding displacement
 194 l_{\max} , respectively. These two analytical solutions are derived in what follows and verified in section 5.4.

195 *4.3.1. Dynamic responses of structure-cladding system*

196 Considering a structure base-excited by a zero-mean stochastic stationary Gaussian process, the peak
 197 response $q_{s,\max}$ of a structure subjected to a ground motion of zero-mean stationary Gaussian process is
 198 given by [65, 75]

$$\begin{aligned}
q_{s,\max} &= \tau \sigma_s \\
\tau &= \sqrt{2 \ln(\nu_e T_e)} + \frac{0.5772}{\sqrt{2 \ln(\nu_e T_e)}} \\
\nu_e &= (1.9 \xi_s^{0.15} - 0.73) \frac{\omega_s}{\pi}
\end{aligned} \tag{31}$$

199 where σ_s is the standard deviation of the structural displacement $q_{s1}(t)$, τ is the peak factor, ν_e is the
200 modified mean zero-crossing rate, and ω_s and ξ_s are the natural frequency and the damping ratio of the
201 fundamental vibration mode, respectively. The variance of the structural displacement σ_s^2 is obtained by
202 integrating the product of the excitation PSDF $G(\omega)$ and the transfer function of the structure-cladding model
203 $H_s(\lambda)$ [64, 76]. Assuming that the response power spectrum of a lightly damped structure is dominated by
204 the contribution of the excitation around that of the natural frequency of the structure, a constant excitation
205 power spectrum $G(\omega_s)$ around the first natural frequency of the structure ω_s is used to compute σ_s^2 [77, 78]

$$\sigma_s^2 = \frac{1}{\omega_s^4} \int_0^{+\infty} |H_s(\lambda)|^2 G(\omega) d\omega = \frac{G(\omega_s)}{2\omega_s^3} J_s \tag{32}$$

with

$$J_s = \int_{-\infty}^{+\infty} |H_s(\lambda)|^2 d\lambda \tag{33}$$

206 A solution for J_s can be obtained using the integral formula from Gradshteyn and Ryzhik [79], as
207 summarized in Appendix Eq. 62. It has been found that the higher mode effects on seismic response of
208 floor acceleration are non-negligible even for first-mode dominated structures, but that inter-story drifts
209 are affected significantly less [80]. Here, we simplify the design problem by only considering the maximum
210 inter-story drift ratio from the first mode shape

$$\Delta_{\max} = \max_i \left| \frac{\phi_{s,1i} - \phi_{s,1i-1}}{h_i} \right| q_{s,\max} \tag{34}$$

211 where h_i is the inter-story height of the i^{th} floor. The non-dimensional analytical solution R_s is defined by
212 the maximum inter-story drift ratio of the structure

$$R_s = \frac{\Delta_{\max}}{\max_i \left| \frac{\phi_{s,1i} - \phi_{s,1i-1}}{h_i} \right| m_{se} \hat{x}_g / k_{se}} = \frac{\tau}{\hat{x}_g} \sqrt{\frac{G(\omega_s) \omega_s}{2}} J_s \tag{35}$$

213 Similarly, the maximum relative displacement structure-cladding l_{\max} is written

$$l_{\max} = \max_i |\tau \sigma_{ci}| \tag{36}$$

214 where σ_{ci} is the standard deviation of the relative displacement of the i^{th} cladding to the primary structure
215 $q_{c1,i}(t)$. The corresponding variance σ_{ci}^2 is given by

$$\sigma_{ci}^2 = \frac{G(\omega_s)}{2\omega_s^3} \int_{-\infty}^{+\infty} |H_{ci}(\lambda)|^2 d\lambda = \frac{G(\omega_s)}{2\omega_s^3} J_{ci} \tag{37}$$

216 with the solution of the integral of the transfer function associated with structure-cladding displacement
 217 $J_{ci} = \int_{-\infty}^{+\infty} |H_{ci}(\lambda)|^2 d\lambda$ solved in Appendix. The maximum structure-cladding spacing is written

$$l_{\max} = \frac{\max_i |\sqrt{J_{ci}}| \tau \sqrt{G(\omega_s)}}{\omega_s \sqrt{2\omega_s}} \quad (38)$$

218 and the non-dimensional analytical solution R_c representing maximum spacing defined as

$$R_c = \frac{l_{\max}}{m_{se} \hat{x}_g / k_{se}} = \frac{\max_i |\sqrt{J_{ci}}| \tau \sqrt{G(\omega_s) \omega_s}}{\hat{x}_g \frac{2}{2}} \quad (39)$$

219 4.3.2. Dynamic parameters for cladding connection

220 The dynamic parameters for the cladding connection are selected based on analytical solutions R_s and
 221 R_c . First, an initial stiffness value k_{ce} is selected by choosing a tuning frequency ratio f

$$k_{ce} = \mu f^2 k_{se} \quad (40)$$

222 Second, the damping ratio of the connection ξ_c is selected through a minimization of the inter-story drift
 223 ratio given f . Using Eq. 33, an estimated value for ξ_c is obtained by setting $\partial J_s / \partial \xi_c = 0$. For simplicity,
 224 we take structural damping $\xi_s = 0$ and J_s reduces to

$$J_s = \frac{\pi}{2f\mu\Gamma_2} \left(\frac{\Lambda_{c1}}{\xi_c} + \xi_c \Lambda_{c2} \right) \quad (41)$$

225 where parameters Λ_{c1} and Λ_{c2} are independent of the damping ratio ξ_c with $\Lambda_{c1} = \Gamma_m^2 - 2(1 + \mu\Gamma_2)(\mu\Gamma_1 +$
 226 $\Gamma_m)\Gamma_m f^2 + (\mu\Gamma_1 + \Gamma_m)^2 f^2 [(1 + \mu\Gamma_2)^2 f^2 + \mu\Gamma_2]$ and $\Lambda_{c2} = 4(1 + \mu\Gamma_2)(\mu\Gamma_1 + \Gamma_m)^2 f^2$. Applying $\partial J_s / \partial \xi_c = 0$
 227 gives

$$\xi_c = \sqrt{\frac{(1 + \mu\Gamma_2)f^2}{4} + \frac{\Gamma_m^2}{4(1 + \mu\Gamma_2)(\mu\Gamma_1 + \Gamma_m)^2 f^2} + \frac{(\mu\Gamma_1 + \Gamma_m)\mu\Gamma_2 - 2\Gamma_m(1 + \mu\Gamma_2)}{4(1 + \mu\Gamma_2)(\mu\Gamma_1 + \Gamma_m)}} \quad (42)$$

228 Note that structural damping is not considered to be negligible ($\xi_s \neq 0$) in the computation of the peak
 229 building responses using analytical solutions R_s and R_c . Afterwards, the computed peak building responses
 230 are compared against the performance metrics. If $\Delta_{\max} \leq \Delta_p$ and $l_{\max} \leq l_c$, the design phase is completed.
 231 Otherwise, an iteration will be conducted through altering the design parameters k_{ce} , ξ_c and/or l_c until
 232 the performance objectives are achieved. Lastly, the friction damping capacity F_{cp} at each connection is
 233 obtained using Eq. 8. In the equivalent damping representations, the VFCC damping is equivalent to
 234 viscous damping element under a harmonic excitation acting on the first natural frequency of the structure
 235 ω_s and the amplitude of structure-cladding displacement taken as $\hat{x} = l_{\max}$

$$F_{cp} = \frac{1}{4} \pi m_{ce} \omega_c \omega_s (\xi_c - \xi_{c0}) l_{\max} \quad (43)$$

with

$$\xi_{c0} = \frac{c_{c0}}{2m_{ce}\omega_c} \quad (44)$$

236 **5. Numerical Simulations**

237 Two steel moment-resisting frame structures are used for numerical simulations to verify and demonstrate
 238 the proposed MBD procedure. They consist of a 5-story building [81] and a 20-story building [82] found in
 239 the literature, but they are assumed to be located in Los Angeles, CA, for seismic design. These example
 240 buildings are modeled as lumped-mass shear systems with their dynamic properties listed in Tables 3 and
 241 4. The fundamental structural damping ratio ξ_s is assumed to be 2% for each building. The total length
 242 of the cladding panels at each floor for the 5-story and 20-story building are 24 m and 36.6 m, respectively.
 243 The cladding elements are concrete panels with 30% window opening area, the densities of the concrete and
 244 glass taken as 2,400 kg/m³ and 2,800 kg/m³, respectively. The thicknesses of the concrete and glass window
 245 panels are taken as 15 cm and 0.8 cm, respectively [83], used for the computation of the cladding’s mass for
 246 each building in Tables 3 and 4. The cladding-floor mass ratio m_{ci}/m_{si} of each floor are also listed in the
 247 Tables. Note that the cladding-structure mass ratio $\mu = m_{ce}/m_{se}$ refers to the equivalent masses of the
 248 structure and cladding, different from the cladding-floor mass ratio m_{ci}/m_{si} defined here.

Table 3: Dynamic parameters - 5-story building.

floor	height (m)	mass (kg)	stiffness (kN/m)	cladding mass (kg)	mass ratio
5	3.6	266,100	84,000	22,400	0.083
4	3.6	204,800	89,000	22,400	0.108
3	3.6	207,000	99,000	22,400	0.107
2	3.6	209,200	113,000	22,400	0.105
1	4.2	215,200	147,000	26,100	0.102

Table 4: Dynamic parameters - 20-story building.

floor	height (m)	mass (kg)	stiffness (kN/m)	cladding mass (kg)	mass ratio
20	3.96	584,000	100,576	37,500	0.064
19	3.96	552,000	133,952	37,500	0.068
18	3.96	552,000	164,416	37,500	0.068
17	3.96	552,000	178,752	37,500	0.068
16	3.96	552,000	197,568	37,500	0.068
15	3.96	552,000	200,928	37,500	0.068
14	3.96	552,000	203,392	37,500	0.068
13	3.96	552,000	232,064	37,500	0.068
12	3.96	552,000	236,096	37,500	0.068
11	3.96	552,000	244,832	37,500	0.068
10	3.96	552,000	265,888	37,500	0.068
9	3.96	552,000	270,592	37,500	0.068
8	3.96	552,000	273,952	37,500	0.068
7	3.96	552,000	277,088	37,500	0.068
6	3.96	552,000	279,552	37,500	0.068
5	3.96	552,000	275,072	37,500	0.068
4	3.96	552,000	297,920	37,500	0.068
3	3.96	552,000	299,712	37,500	0.068
2	3.96	552,000	304,192	37,500	0.068
1	5.49	563,000	225,568	52,000	0.092

249 The equations of motion of an n -story building equipped with a cladding system has the form:

$$\mathbf{M}\ddot{\mathbf{x}} + \mathbf{C}\dot{\mathbf{x}} + \mathbf{K}\mathbf{x} = -\mathbf{M}\mathbf{E}_g\ddot{x}_g + \mathbf{E}_f\mathbf{F} \quad (45)$$

250 where $\mathbf{x} \in \mathbb{R}^{3n \times 1}$ is the displacement vector, $\mathbf{M} \in \mathbb{R}^{3n \times 3n}$, $\mathbf{C} \in \mathbb{R}^{3n \times 3n}$, and $\mathbf{K} \in \mathbb{R}^{3n \times 3n}$ are the mass,
251 damping, and stiffness matrices of the building, respectively, $\mathbf{F} \in \mathbb{R}^{2n \times 1}$ is the control input vector, \ddot{x}_g is
252 the ground acceleration input, $\mathbf{E}_f \in \mathbb{R}^{3n \times 2n}$ and $\mathbf{E}_g \in \mathbb{R}^{3n \times 1}$ are the control input and ground acceleration
253 input location matrices, respectively.

254 The state-space representation of Eq. 45 for the simulations is written

$$\dot{\mathbf{X}} = \mathbf{A}\mathbf{X} + \mathbf{B}_g\ddot{x}_g + \mathbf{B}_f\mathbf{F} \quad (46)$$

255 where $\mathbf{X} = [\mathbf{x} \quad \dot{\mathbf{x}}]^T \in \mathbb{R}^{6n \times 1}$ is the state vector and with

$$\mathbf{A} = \begin{bmatrix} \mathbf{0} & \mathbf{I} \\ -\mathbf{M}^{-1}\mathbf{K} & -\mathbf{M}^{-1}\mathbf{C} \end{bmatrix}_{6n \times 6n} \quad (47)$$

$$\mathbf{B}_f = \begin{bmatrix} \mathbf{0} \\ \mathbf{M}^{-1}\mathbf{E}_f \end{bmatrix}_{6n \times 2n} \quad (48)$$

$$\mathbf{B}_g = \begin{bmatrix} \mathbf{0} \\ -\mathbf{E}_g \end{bmatrix}_{6n \times 1} \quad (49)$$

256 The numerical algorithm follows the discrete form of the Duhamel integral [1]:

$$\mathbf{X}(t + \Delta_t) = e^{\mathbf{A}\Delta_t}\mathbf{X}(t) + \mathbf{A}^{-1}(e^{\mathbf{A}\Delta_t} - \mathbf{I})[\mathbf{B}_f\mathbf{F}(t) + \mathbf{B}_g\ddot{x}_g(t)] \quad (50)$$

257 where Δ_t is the discrete time interval and $\mathbf{I} \in \mathbb{R}^{6n \times 6n}$ is the identity matrix. This discrete state-space
 258 linear formulation is used to simulate the dynamic responses of the linear structural system with the nonlinear
 259 damping force $\mathbf{F}(t)$. In the simulations, the nonlinear damping force from the VFCC is simulated using the
 260 LuGre friction model (Eq.3). For the semi-active scheme, the required control force vector \mathbf{F}_{req} for VFCCs
 261 is given by a linear quadratic regulator (LQR) of full-state feedback

$$\mathbf{F}_{\text{req}} = -\Theta\mathbf{X} \quad (51)$$

262 where $\Theta \in \mathbb{R}^{2n \times 6n}$ is a tuned control gain matrix for the minimization of a performance objective index W

$$W = \frac{1}{2} \int_0^\infty (\mathbf{X}^T \mathbf{U}_x \mathbf{X} + \mathbf{F}^T \mathbf{U}_f \mathbf{F}) dt \quad (52)$$

263 where $\mathbf{U}_x \in \mathbb{R}^{6n \times 6n}$ and $\mathbf{U}_f \in \mathbb{R}^{2n \times 2n}$ are the regulatory and actuation weight matrices, respectively.
 264 The required control force $F_{\text{req},i}(t)$ is not necessarily attainable by a given VFCC device of capacity F_{cp} . A
 265 bang-bang type controller is used to adjust the actual control force $F_{\text{act},i}(t)$ of the device, where

$$F_{\text{act},i}(t) = \begin{cases} F_{\text{req},i}(t) & \text{if } F_{cp} > |F_{\text{req},i}(t)| \text{ and } F_{\text{req},i}(t) \cdot \dot{x}_{c,i}(t) > 0 \\ F_{cp} & \text{if } F_{cp} \leq |F_{\text{req},i}(t)| \text{ and } F_{\text{req},i}(t) \cdot \dot{x}_{c,i}(t) > 0 \\ 0 & \text{if } F_{\text{req},i}(t) \cdot \dot{x}_{c,i}(t) \leq 0 \end{cases} \quad (53)$$

266 This actual control force $F_{\text{act},i}(t)$ is then converted to a corresponding voltage sent to the linear actuator
 267 acting on the toggles, yielding the kinetic friction force $F_{c,i}(t) = F_{\text{act},i}(t)$. Note that the design and
 268 optimization of the controller is out-of-the-scope of this work. When the VFCC is subjected to multiple
 269 hazards, other control techniques could be utilized, such as adaptive data-driven techniques (see Refs. [48,
 270 84, 85] for instance). In the later numerical simulation, the regulatory and actuation weight matrices are
 271 pre-tuned to $\mathbf{U}_x = \text{diag}[\mathbf{I}_{8 \times 8} \quad 400\mathbf{I}_{2 \times 2} \quad 1000\mathbf{I}_{2 \times 2} \quad 1400\mathbf{I}_{3 \times 3} \quad 600 \quad 1000 \quad 1100 \quad 1500 \quad 550 \quad \mathbf{I}_{10 \times 10}]$ and
 272 $\mathbf{U}_f = 5 \times 10^{-10}\mathbf{I}_{10 \times 10}$ for the 5-story building, and $\mathbf{U}_x = \text{diag}[\mathbf{I}_{35 \times 35} \quad 5\mathbf{I}_{13 \times 13} \quad 10\mathbf{I}_{4 \times 4} \quad 30\mathbf{I}_{8 \times 8} \quad 100\mathbf{I}_{4 \times 4}$
 273 $50\mathbf{I}_{10 \times 10} \quad \mathbf{I}_{46 \times 46}]$ and $\mathbf{U}_f = 5 \times 10^{-9}\mathbf{I}_{10 \times 10}$ for the 20-story building. The weight matrices were pre-tuned
 274 offline here to obtain good mitigation performance of the VFCC. However, the tuning range of these weight
 275 matrices are arbitrarily selected and more optimal solutions may exist for better mitigation performance.

276 The performance of the VFCC with the LQR controller (semi-active case or LQR) is compared against that
 277 of a conventional stiffness connection (uncontrolled case or UN) and the passive VFCC under a constant
 278 maximum capacity (passive-on case or ON). In the uncontrolled case, conventional stiffness connections
 279 are used with tie-back connectors at the top and bearing connectors at the bottom of cladding panels. The
 280 lateral stiffnesses of each tie-back connector and bearing connector are taken as 39 kN/mm and 2335 kN/mm,
 281 respectively [83]. A total number of four cladding panels and twelve cladding panels are installed at each
 282 floor for the 5-story and 20-story buildings, respectively, with each panel connected to the structural system
 283 by two connectors both at the top and bottom. The stiffness element of the lateral connection k_c is taken
 284 as the sum of these connectors at each floor.

285 5.1. Verification of SDOF simplification for cladding system

286 Before conducting numerical simulations on buildings, the model assumption that a 2DOF cladding
 287 system could be reduced into an SDOF representation is first verified. This is done on a simplified 4DOF
 288 representation of the 5-story building. Recall that the purpose of the 4DOF representation is only to verify
 289 the assumptions and does not necessarily represent the dynamics of the 5-story building. The 4DOF system
 290 consists of two identical structural floors and spanned with a cladding panel, as illustrated in Fig. 7(a). The
 291 mass elements of the 4DOF model are obtained by lumping the five structural masses of the 5-story building
 292 into both floors and the five cladding masses into one. The stiffness elements of the 4DOF model are taken
 293 as identical and are computed by setting the fundamental frequency equal to that of the 5-story building
 294 ($\omega_s = 6.33$ rad/s), with a structural damping ratio of $\xi_s = 2\%$. Using the model simplification methodology
 295 (Section 3), an equivalent 2DOF representation is obtained (Fig.7(b)). Table 5 lists the resulting dynamic
 296 parameters. The magnitudes of analytical transfer functions H_s and H_c (Eqs.21 and 22) for the equivalent
 297 2DOF model are written

$$\begin{aligned}
 H_s &= \sqrt{\frac{[\alpha\mu f^2 + \Gamma(f^2 - \lambda^2)]^2 + [2\xi_c f \lambda (\alpha\mu + \Gamma)]^2}{[(1 - \lambda^2)(f^2 - \lambda^2) - 4\xi_c \xi_s f \lambda^2 - \alpha^2 \mu f^2 \lambda^2]^2 + [2\xi_c f \lambda (1 - (1 + \alpha^2 \mu) \lambda^2) + 2\xi_s \lambda (f^2 - \lambda^2)]^2}} \\
 H_c &= \sqrt{\frac{(1 - \lambda^2 + \alpha \Gamma \lambda^2)^2 + (2\xi_s \lambda)^2}{[(1 - \lambda^2)(f^2 - \lambda^2) - 4\xi_c \xi_s f \lambda^2 - \alpha^2 \mu f^2 \lambda^2]^2 + [2\xi_c f \lambda (1 - (1 + \alpha^2 \mu) \lambda^2) + 2\xi_s \lambda (f^2 - \lambda^2)]^2}} \quad (54)
 \end{aligned}$$

298 where $\alpha = \frac{\phi_{s,11} + \phi_{s,12}}{2\phi_{s,12}}$ and $\Gamma = \sum_{i=1}^2 \frac{\phi_{s,1i} m_{si}}{\phi_{s,12} m_{se}}$. In simulations, the friction damping element F_c at the 4DOF
 299 system is modeled as a passive Coulomb friction element and its capacity is taken as $F_c = \frac{\pi}{4} f \lambda \xi_v H_c m_{ce} \ddot{x}_{g0}$,
 300 equivalent to the viscous damping element of a damping ratio ξ_v . The total viscous damping ratio of the
 301 cladding connection ξ_c is taken as $\xi_c = \xi_v + \xi_{c0}$, with the inherent viscous damping ratio $\xi_{c0} = \frac{c_{c0}}{2\sqrt{k_{ce} m_{ce}}} = 2\%$.

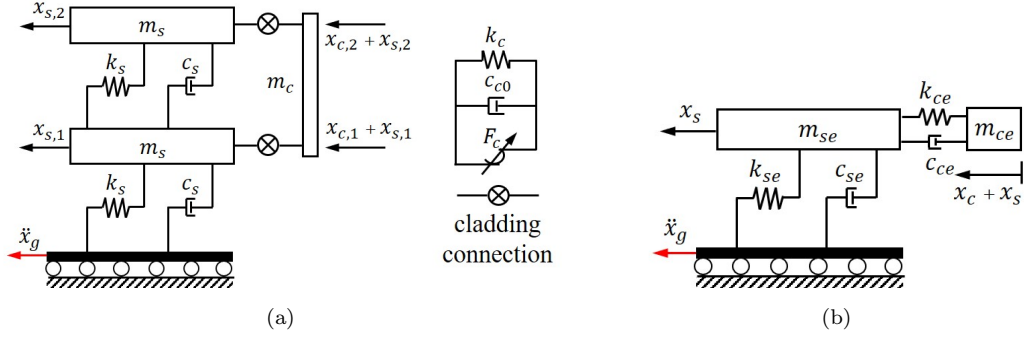


Figure 7: Representation of structure-cladding system: (a) 4DOF; and (b) 2DOF.

Table 5: Dynamic parameters for the 4DOF and 2DOF representations.

	parameter	value	unit
4DOF	m_s	551150	kg
	k_s	57890	$\text{kN}\cdot\text{m}^{-1}$
	c_s	366	$\text{kN}\cdot\text{s}\cdot\text{m}^{-1}$
	m_c	110230	kg
2DOF	m_{se}	761670	kg
	k_{se}	30558	$\text{kN}\cdot\text{m}^{-1}$
	c_{se}	193	$\text{kN}\cdot\text{s}\cdot\text{m}^{-1}$
	m_{ce}	110230	kg

302 The verification is conducted through a comparison of transfer function plots obtained from the equivalent
 303 2DOF model (i.e., analytical solution) and from the 4DOF model (i.e., numerical solution). Figs. 8 to
 304 9 plot the magnitudes of transfer functions H_s and H_c , with a tuning frequency ratio $f = 0.9$ which
 305 represents a tuning around the structure's natural frequency, and with two representative damping cases
 306 $\xi_v = \frac{c_v}{2\sqrt{k_{ce}m_{ce}}} = 10\%$ and $\xi_v = 50\%$ to investigate the effect of the damping of the connection. Results show
 307 a general good fit of the numerical solution, except around the second resonant frequency ratio $\lambda = 2.5$,
 308 because the second mode of the primary structure is not modeled in the analytical solution. The disagreement
 309 in the fit increases at relatively high damping ($\xi_v = 50\%$), especially under H_c . This can be attributed to the
 310 discontinuous motion induced by the stick-slip behavior that becomes more important, whereas the viscous
 311 damping equivalence assumption does not hold strongly. It follows that the analytical solutions are a good
 312 approximation of the system, but that additional care must be taken in the design process for large values
 313 of ξ_v .

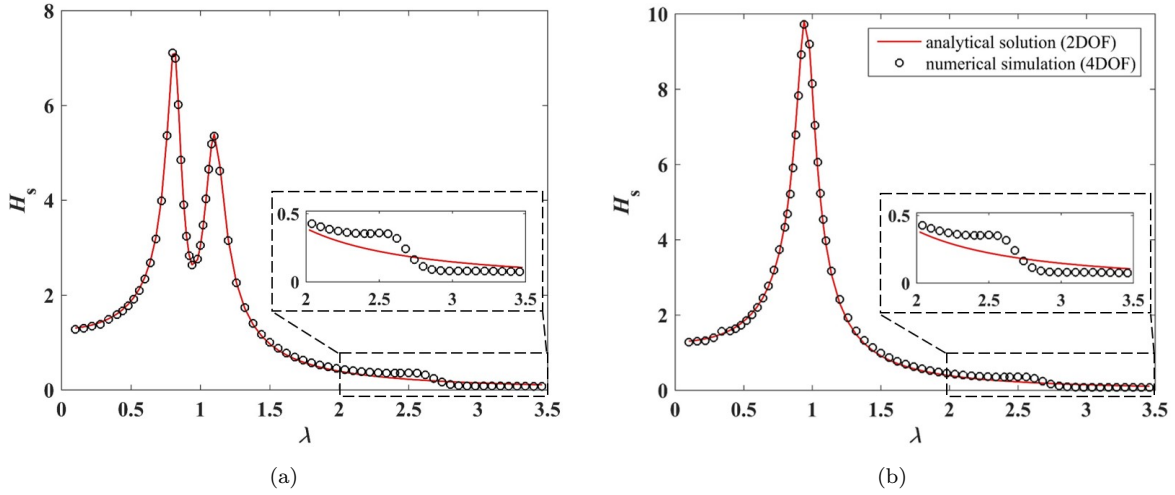


Figure 8: Analytical versus numerical solutions for transfer function H_s at $f = 0.9$, (a) $\xi_v = 10\%$ and (b) $\xi_v = 50\%$.

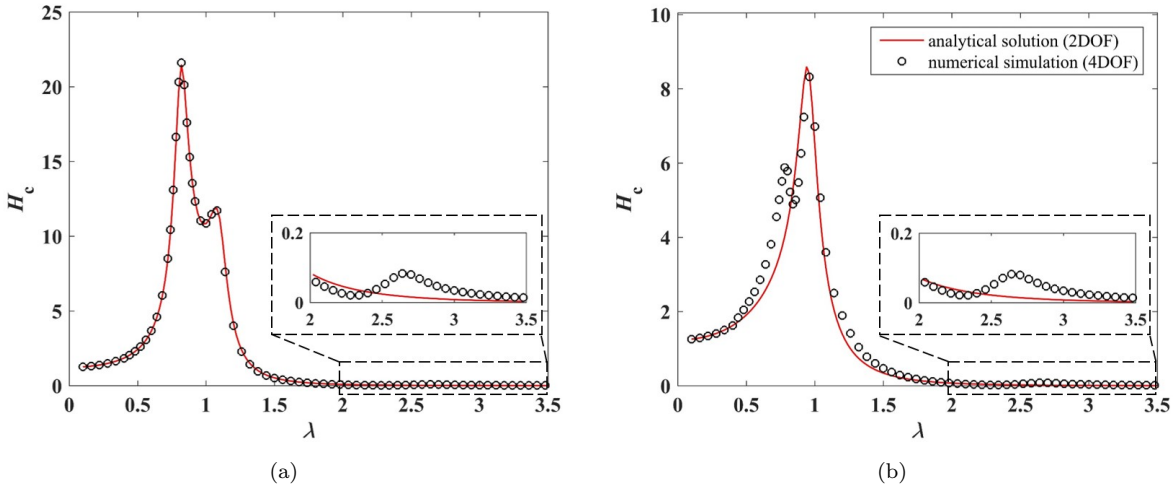


Figure 9: Analytical versus numerical solutions for transfer function H_c at $f = 0.9$, (a) $\xi_v = 10\%$ and (b) $\xi_v = 50\%$.

314 Next, parametric studies are conducted to further investigate the effect of dynamic parameters on the
 315 responses. The investigated parameters include mass ratio μ (Fig. 10), tuning frequency ratio f (Fig. 11),
 316 and damping ratio ξ_c (Fig. 12). These studies are performed using the analytical solutions verified above (Eq.
 317 54). Fig. 10 plots the transfer functions associated with floor displacements (H_s) and structure-cladding
 318 displacements (H_c) over a range of the mass ratios μ from 0.01 to 0.1 based on a typical mass ratio of a tuned
 319 mass damper system. The actual cladding-structure mass ratio μ varies on buildings given the architectural
 320 requirements, and it may not always be possible to attain the ideal values. Nevertheless, different cladding
 321 masses can be achieved through the use of different materials such as glass, masonry or precast concrete

322 panels or adjusting cladding's thickness, yielding mass ratios as high as 0.1 [86]. Results show that an
 323 increasing mass ratio leads to a better mitigation performance for both H_s and H_c , as expected from the
 324 theory of tuned mass dampers [1]. Double humps that start to appear in H_s for larger values of μ are also
 325 observable, exhibiting the modal frequency of the added mass. Fig. 11 (a) plots the effect of decreasing
 326 the connection stiffness, starting with the typical stiffness or a traditional connection. Results show that,
 327 analogous to tuned mass dampers, there exists an optimal value for f that minimizes H_s , but that a more
 328 flexible cladding connection increases H_c , as observable in Fig. 11(b). This may cause the cladding system
 329 to exceed the allowable structure-cladding displacement. Also, observable double humps in H_s occur once
 330 the frequency ratio f is tuned around the structure's natural frequency. Fig.12 plots results for ξ_c , also
 331 showing that an optimal value exists for the optimal mitigation of H_s .

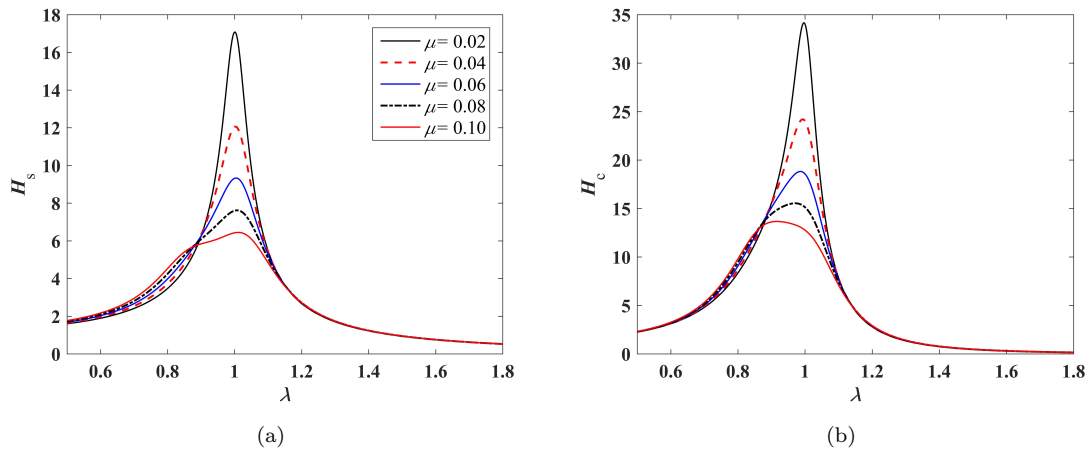


Figure 10: Plots of analytical transfer functions under various mass ratios μ at $f = 0.9$ and $\xi_c = 20\%$: (a) H_s ; and (b) H_c .

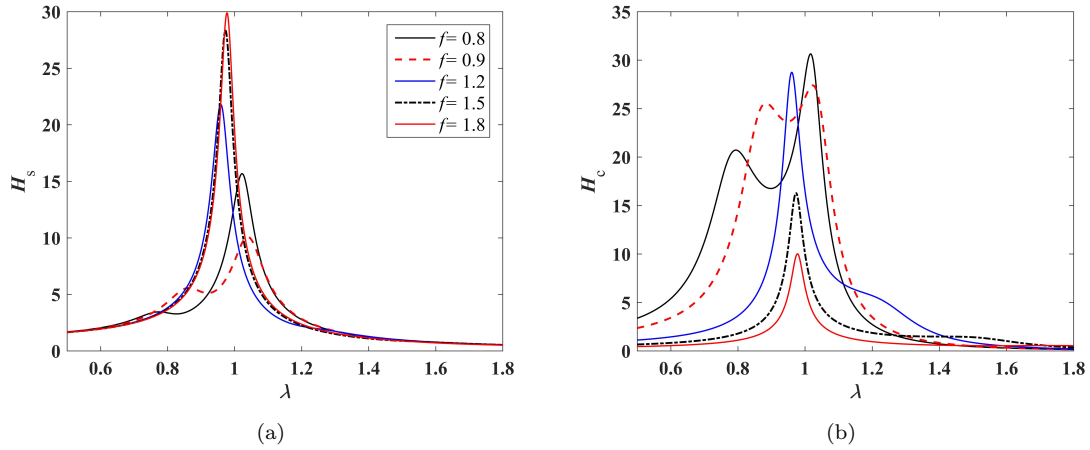


Figure 11: Plots of analytical transfer functions under various tuning frequency ratios f at $\mu = 0.05$ and $\xi_c = 10\%$: (a) H_s ; and (b) H_c .

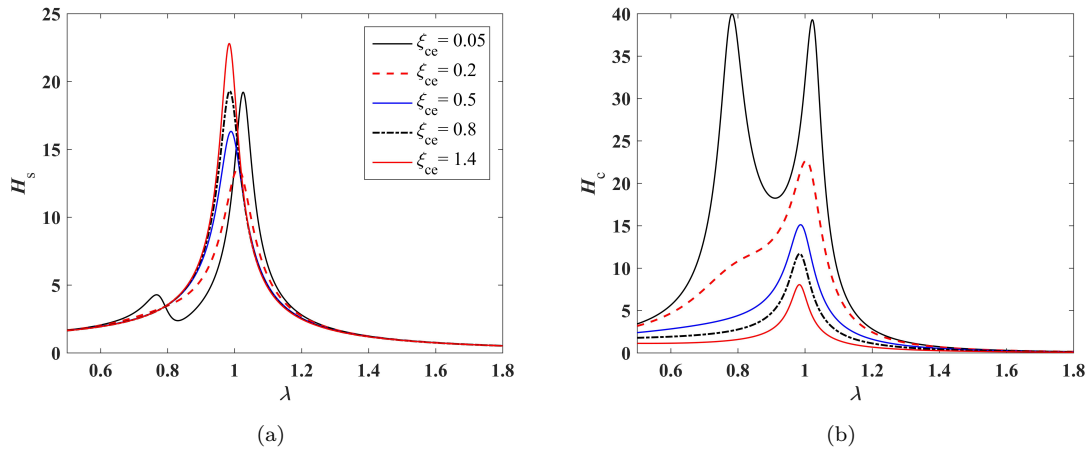


Figure 12: Plots of analytical transfer functions under various connection damping ratios ξ_c at $\mu = 0.05$ and $f = 0.8$: (a) H_s ; and (b) H_c .

332 5.2. Demonstration of MBD procedure

333 In this section, the proposed MBD procedure is demonstrated on the two selected buildings. The seismic
 334 hazard is quantified, followed by the determination of performance objectives and the design of the connection
 335 parameters.

336 Seismic Hazard Quantification

337 First, the local design response spectra of the buildings are established using the spectral acceleration
 338 parameters S_{DS} and S_{D1} extracted from the USGS seismic design map, corresponding to a structural

339 damping ratio of $\xi_s = 2\%$. These parameters are listed in Table 6. Both the 5-story and 20-story buildings
 340 are assumed to be designed based on the local design spectra in Los Angeles, CA. Fig. 13(a) plots the
 341 updated discrete design spectrum compatible PSDF $G_{\text{new}}(\omega_N)$ and Fig. 13(b) compares the target $S_g(\xi_s)$
 342 (ASCE7-10) and simulated $S_g(\xi_s)$ (Section 4.1). Corresponding values for the PSDF $G(\omega_s)$ around the
 343 fundamental frequency of each building are listed in Table 6.

Table 6: Design spectral acceleration parameters.

parameters	unit	5-story	20-story
S_{DS}	g	0.827	0.827
S_{D1}	g	0.428	0.428
ω_s	rad·s ⁻¹	6.334	1.662
$G(\omega_s)$	m ² ·s ⁻³	0.029	0.011

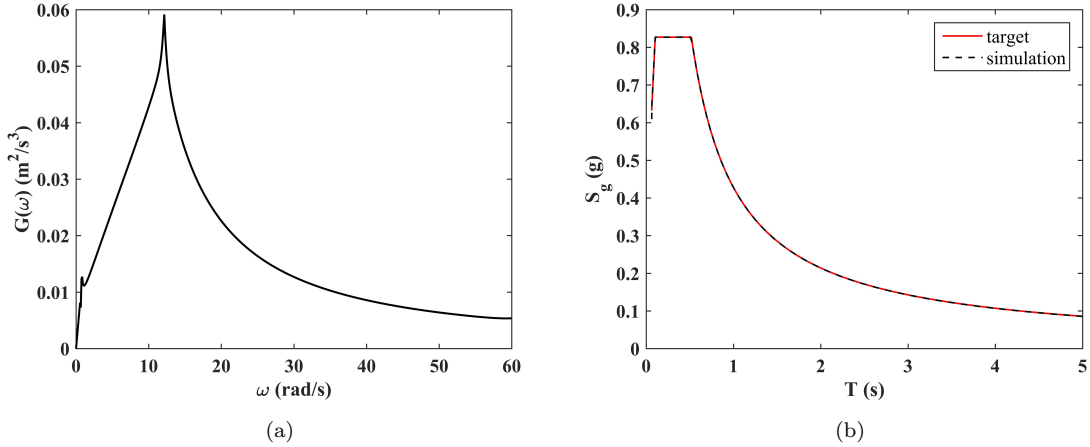


Figure 13: (a) Design spectrum compatible PSDF $G(\omega)$; and (b) response spectrum S_g .

344 Performance Objectives

345 Using values listed in Section 4.2, a range of $\Delta_p < 1.0\%$ is selected to maintain an elastic state [73]. A
 346 preliminary value for the maximum structure-cladding spacing l_c is set to 0.25 m, with a maximum upper
 347 bound set as high as 1 m based on values reported in Ref. [34].

348 Connection Design

349 Values of the equivalent mass m_{se} and stiffness k_{se} of the primary structure are listed in Table 7 for each
 350 building, as well as the mass ratio μ . The peak responses of the two selected buildings are estimated using
 351 R_s and R_c with an arbitrary $\hat{x}_g = 1\text{m/s}^2$. Note that Δ_{max} and l_{max} are first computed using Eqs. 34 and 38
 352 that are independent on \hat{x}_g . Non-dimensional solutions R_s and R_c are then introduced with an arbitrarily

353 $\widehat{\ddot{x}}_g$ that does not need to represent the actual ground acceleration.

354 Using Eq.34 and Eq.38, Fig. 14 plots the estimated peak responses of each building against various tuning
 355 frequency ratios f to facilitate the selection of connection parameters. A tuning frequency ratio $f = 1.01$ is
 356 selected for the 5-story building, yielding the equivalent connection stiffness $k_{ce} = \mu f^2 k_{se} = 9.46 \times 10^5$ N/m,
 357 connection damping ratio $\xi_c = 0.16$ (Eq.42), and the total friction capacity of the VFCCs at each floor
 358 $F_{cp} = 25.5$ kN (Eq.43). This yields $R_s = 4.95$ and $R_c = 9.88$ (Eqs. 35 and 39). These design parameters
 359 result in $\Delta_{\max} = 0.82\% \leq 1\%$ and the maximum structure-cladding spacing $l_{\max} = 0.25$ m $\leq l_c = 0.25$ m,
 360 satisfying the performance objectives.

361 A tuning frequency ratio $f = 1.63$ initially selected for the 20-story building yields an unsatisfied
 362 performance of the maximum inter-story drift ratio $\Delta_{\max} = 1.11\% > 1\%$. The design process is iterated
 363 by increasing the allowable structure-cladding spacing l_c to 0.42 m to introduce a more flexible connection
 364 (i.e., lowering f). The tuning frequency ratio is reduced to $f = 1.33$, giving the equivalent connection
 365 stiffness $k_{ce} = \mu f^2 k_{se} = 1.87 \times 10^5$ N/m, connection damping ratio $\xi_c = 0.37$ (Eq.42), and the total
 366 friction capacity at each floor $F_{cp} = 16.0$ kN (Eq.43). The corresponding values for non-dimensional
 367 analytical solutions are $R_s = 1.69$ and $R_c = 1.19$ (Eqs. 35 and 39), giving $\Delta_{\max} = 1\% \leq 1\%$ and
 368 $l_{\max} = 0.42$ m $\leq l_c = 0.42$ m, satisfying the performance objectives. The cladding connection parameters
 369 are listed in Table 7.

Table 7: Cladding connection design parameters.

parameters	variable	unit	note	value	
				5-story	20-story
dynamic parameters	m_{se}	10^3 kg	Eq.16	564	5,057
	k_{se}	$\text{kN}\cdot\text{m}^{-1}$	Eq.16	22,618	1,397
	μ	%	Eq.20	4.10	0.76
performance objectives	Δ_p	%	–	0.83	1.00
	l_c	m	–	0.25	0.42
design parameters	f	–	–	1.01	1.33
	ξ_c	–	–	0.16	0.37
	R_s	–	Eq.35	4.95	1.69
	R_c	–	Eq.39	9.88	1.19
	k_{ce}	$\text{kN}\cdot\text{m}^{-1}$	Eq.40	946	187
	F_{cp}	kN	Eq.43	25.5	16.0

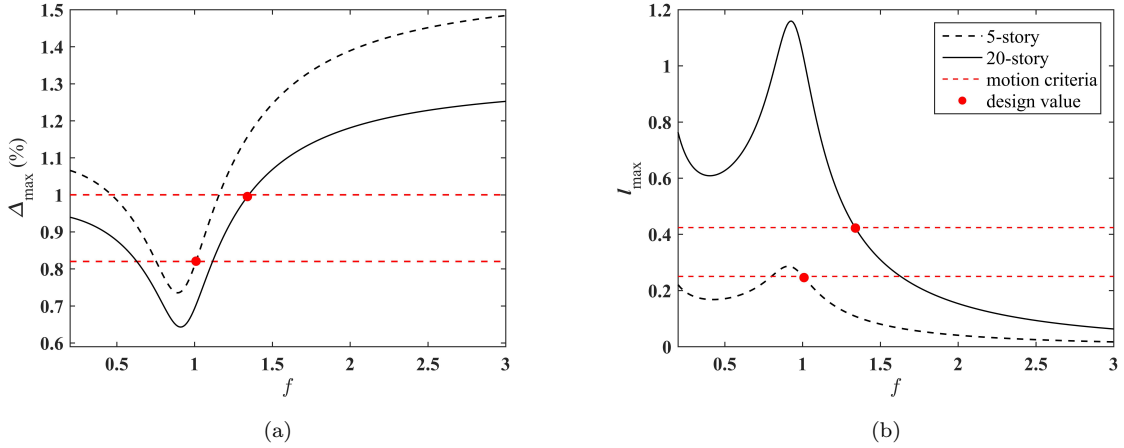


Figure 14: Peak responses of selected buildings as a function of f : (a) Δ_{\max} and (b) l_{\max} .

370 5.3. Seismic loads

371 A set of six different earthquakes were selected for the simulations, among which both near-field and far-
 372 field ground motions are considered. Near-field and far-field earthquakes are defined based on the epicentral
 373 distance, with 0 to 50 km associated with near-field and 50 km and beyond associated with far-field. Time
 374 series data of these ground motions were extracted from the PEER ground motion record database [87] and
 375 their dynamic characteristics are listed in Table 8. Original ground motions were scaled to the local design
 376 response spectrum at the fundamental period of each building with a structural damping ratio $\xi_s = 2\%$
 377 , yielding the corresponding scaling factors in Table 8. The scaled ground motion and design response
 378 spectrum are plotted in Fig. 15.

Table 8: Selected seismic excitations.

	hazard	location	year	station	dist (km)	mechanism	scale factor	
							5-story	20-story
far-field	EQ1	Northridge	1994	West Covina	51.46	reverse	0.76	0.95
	EQ2	Kern County	1952	Hollywood Stor FF	114.62	reverse	0.71	0.47
	EQ3	Landers	1992	Arcadia	135.22	strike-slip	0.97	0.70
near-field	EQ4	Kobe	1995	Port Island	3.31	strike-slip	1.02	1.18
	EQ5	San Fernando	1971	Hollywood Stor FF	22.77	reverse	0.98	0.53
	EQ6	Loma Prieta	1989	Agnews State Hospital	24.27	reverse-oblique	0.77	0.68

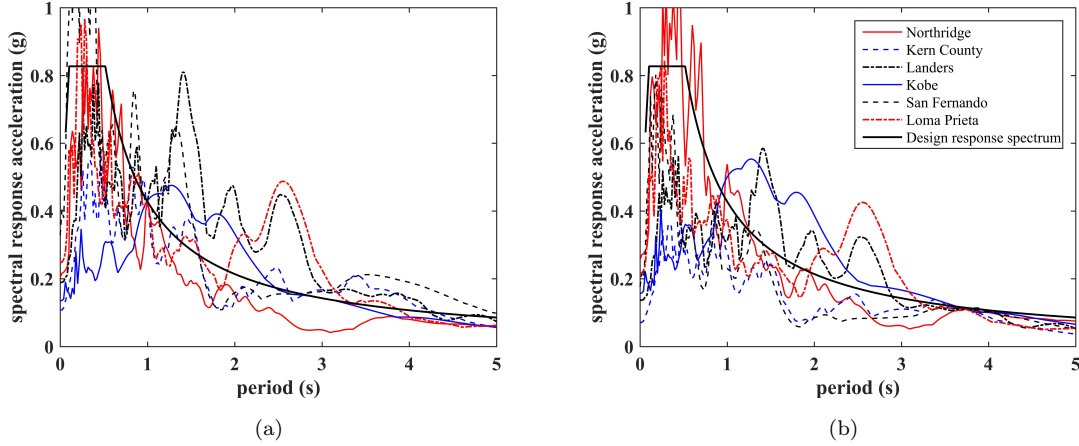


Figure 15: Scaled response spectra of selected seismic excitations : (a) 5-story (fundamental period: $T_s = 0.99$ s); and (b) 20-story (fundamental period: $T_s = 3.78$ s).

379 5.4. Simulation results

380 Two performance indices are defined to evaluate the VFCC's performance:

- Maximum inter-story drift reduction β_s

$$\beta_s = \frac{\max_{i,t} |\Delta_{un,i}(t)| - \max_{i,t} |\Delta_i(t)|}{\max_{i,t} |\Delta_{un,i}(t)|} \quad (55)$$

381 where the controlled inter-story drift ratio $\Delta_i = (x_{s,i} - x_{s,i-1})/h_i$ for $i = 2, 3, \dots, n$, $\Delta_1 = x_{s,1}/h_1$ for
 382 $i = 1$, and $\Delta_{un,i}$ refers to the uncontrolled inter-story drift ratio.

- Maximum absolute acceleration reduction β_a

$$\beta_a = \frac{\max_{i,t} |\ddot{x}_{un,i}(t)| - \max_{i,t} |\ddot{x}_i(t)|}{\max_{i,t} |\ddot{x}_{un,i}(t)|} \quad (56)$$

384 where the absolute acceleration \ddot{x}_i for $i = 1, 2, \dots, n$ is the acceleration for the controlled cases and $\ddot{x}_{un,i}$
 385 is the acceleration for the uncontrolled case.

386 Results for performance indices β_s and β_a are listed in Table 9 for both buildings. Positive values for β_s
 387 and β_a show that the VFCC under both the ON and LQR case dissipates energy. A comparison of β_s and β_a
 388 shows that the semi-active controlled VFCC (LQR) provides significant reductions on buildings' responses.
 389 In particular, the maximum reductions on the peak inter-story drift ratio and the peak absolute acceleration
 390 under the semi-active VFCC scheme reach 53.5% and 48.3%, respectively, for the 5-story building under
 391 hazard EQ2, and 27.8% and 22.5% , respectively, for the 20-story building under hazard EQ3. The
 392 overall mitigation on the 20-story building is less given the higher period of the structure.

Table 9: Simulation results - β_s and β_a .

hazard	5-story building				20-story building			
	$\beta_s(\%)$		$\beta_a(\%)$		$\beta_s(\%)$		$\beta_a(\%)$	
	ON	LQR	ON	LQR	ON	LQR	ON	LQR
EQ1	10.3	43.0	13.2	40.7	5.6	17.6	4.5	5.0
EQ2	11.6	53.5	11.1	48.3	0.9	15.0	0.8	18.2
EQ3	7.2	34.9	6.9	31.4	12.3	27.8	7.6	22.5
EQ4	3.1	22.9	2.5	23.0	6.7	11.2	0.5	5.6
EQ5	7.1	29.2	11.7	26.3	4.6	13.9	3.4	10.3
EQ6	16.7	49.7	8.5	30.1	1.3	10.8	0.1	9.3

393 Figs.16 and 17 plot the maximum response profiles for the 5-story building under hazard EQ3 and 20-
394 story building under hazard EQ2, respectively. These two representative hazard cases are selected because
395 they exhibit an average reduction in the maximum inter-story drift ratio among all hazard cases. Results
396 show that the semi-actively controlled VFCC (LQR) significantly reduces both the maximum inter-story
397 drift ratio and the maximum absolute acceleration, especially for the short 5-story building. In terms of the
398 inter-story drift ratio, the semi-active VFCC is critical in providing a response under the limit threshold.
399 The LQR case generally results in a larger structure-cladding displacement at each floor, as expected. The
400 maximum structure-cladding displacements plotted in Figs.16 (c) and 17 (c) for both the 5-story and 20-story
401 building are below their allowable design values of 0.25 m and 0.42 m, which satisfies the performance
402 metrics.

403 Table 10 compares the design performance criteria and the peak building responses for all hazard cases.
404 Results confirm that the semi-active VFCC (LQR) is capable of bringing the building responses under the
405 design targets, with $\Delta_{\max} \leq 0.82\%$ and $l_{\max} \leq 0.25$ m for the 5-story building, and $\Delta_{\max} \leq 1\%$ and
406 $l_{\max} \leq 0.42$ m for the 20-story building, respectively. The table also compares the median responses (50th
407 percentile) computed assuming a lognormal distribution of the responses [88]. Results show that the semi-
408 active VFCC (LQR) can significantly reduce the response of the inter-story drift to the desirable design level.
409 Remark that the passive-on case often fails at satisfying the design criteria. This phenomenon is studied
410 next.

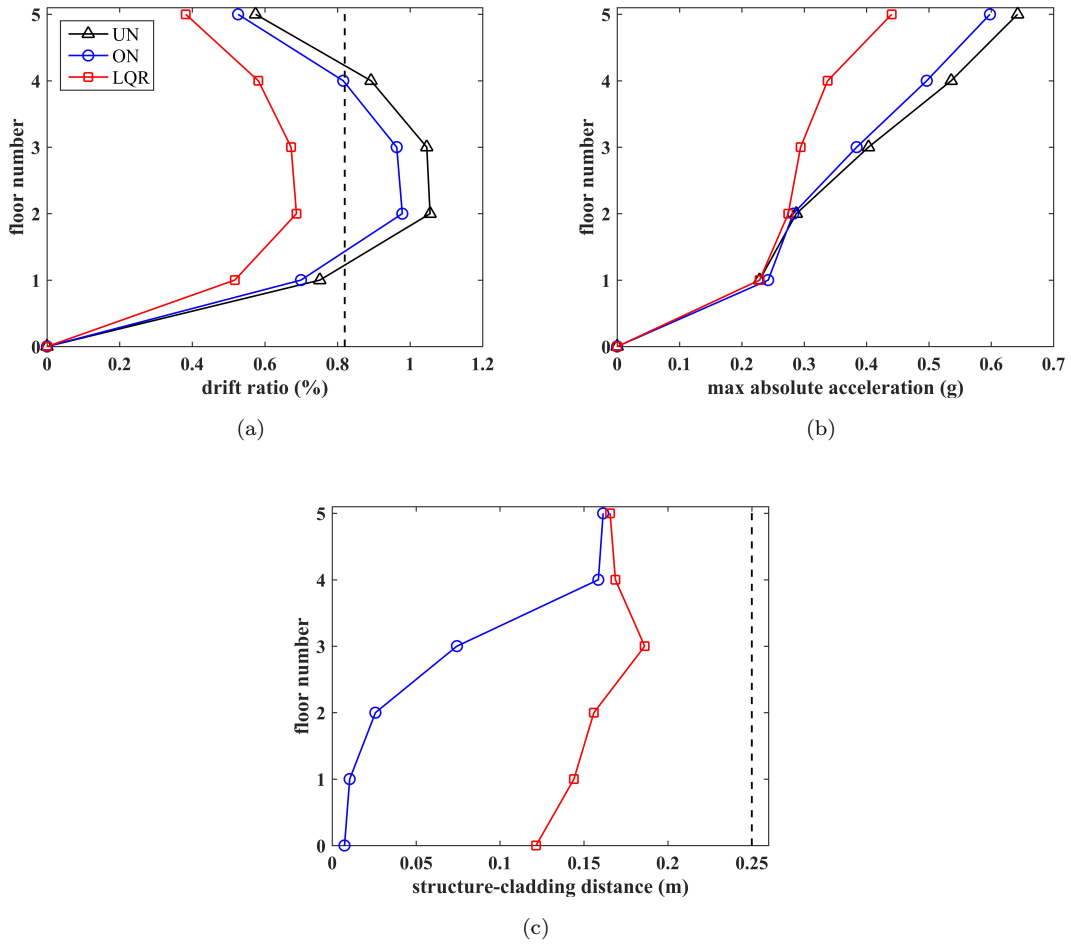


Figure 16: Maximum response profile of 5-story building under hazard EQ3: (a) drift ratio, (b) absolute acceleration, and (c) structure-cladding displacement (uncontrolled case not shown).

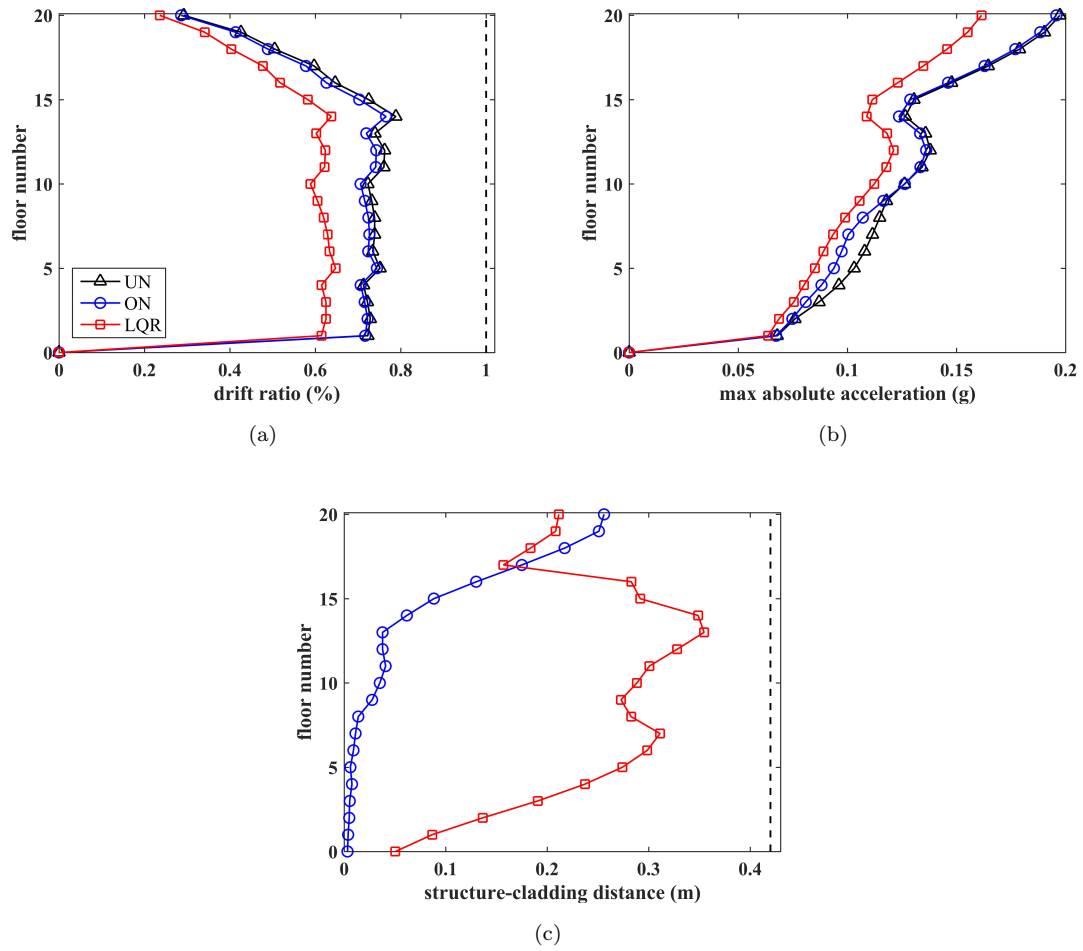


Figure 17: Maximum response profile of 20-story building under hazard EQ2: (a) drift ratio, (b) absolute acceleration, and (c) structure-cladding displacement (uncontrolled case not shown).

Table 10: Results for motion performance criteria.

hazard	5-story building					20-story building				
	$\Delta_{\max}(\%)$			$l_{\max}(\text{m})$		$\Delta_{\max}(\%)$			$l_{\max}(\text{m})$	
	UN	ON	LQR	ON	LQR	UN	ON	LQR	ON	LQR
EQ1	0.85	0.76	0.48	0.10	0.14	0.94	0.89	0.78	0.23	0.34
EQ2	0.84	0.74	0.39	0.09	0.13	0.79	0.77	0.65	0.26	0.35
EQ3	1.06	0.98	0.69	0.16	0.19	1.05	0.95	0.80	0.37	0.39
median far-field	0.91	0.82	0.51	0.11	0.15	0.92	0.87	0.74	0.28	0.36
EQ4	1.00	0.97	0.78	0.12	0.22	1.04	1.00	0.97	0.42	0.41
EQ5	1.00	0.93	0.71	0.11	0.22	0.91	0.86	0.78	0.24	0.37
EQ6	0.89	0.74	0.45	0.11	0.13	0.72	0.71	0.64	0.16	0.36
median near-field	0.96	0.87	0.63	0.11	0.18	0.88	0.85	0.79	0.25	0.38

411 In order to verify the quality of the analytical solutions for design, two non-dimensional analytical solu-
412 tions (R_s and R_c) are plotted in Figs. 18 and 19 for the 5-story and 20-story buildings, respectively. These
413 two non-dimensional analytical solutions are studied for the designed connection stiffness under various
414 damping capacities and compared against the simulation results by introducing performance metric R^* :

$$R^* = \frac{R_{\text{model}} - R_{\text{simulation}}}{R_{\text{model}}} \times 100\%$$

415 where the R refers to R_s and R_c and the subscript ‘model’ denotes the analytical solutions and ‘simulation’
416 denotes numerical solutions, for the controlled cases. Simulation results for the 5-story and 20-story buildings
417 both presented under hazard EQ3, to study the worst case scenarios, whereas each earthquake was
418 associate with the structure’s largest uncontrolled inter-story drifts (Table 10). Significant disagreements
419 can be observed for both R_s and R_c between the passive-on (ON) and the analytical solutions (Model).
420 Results are plotted in Figs. 18 and 19 for the 5-story and 20-story buildings, respectively. R_s is generally
421 underestimated (i.e., $R_s^* < 0$) and R_c overestimated (i.e., $R_c^* > 0$) by the analytical solutions for the 5-storey
422 building. Overestimation of R_s occurs under low damping for the 20-story building, and R_c is overestimated.
423 The high level of error, in particular for the 5-story building, is likely attributed to the neglected nonlinearities
424 from the high friction damping, neglected contributions of the higher modes, and the simplification of seismic
425 load. However, the semi-active case always remains overestimated by the analytical solutions (i.e., $R_s^* > 0$
426 and $R_c^* > 0$). This demonstrates that the MBD procedure yields a conservative design of the VFCC for
427 both selected benchmark buildings when applied in a semi-active regime, consistent with results from Table
428 10.

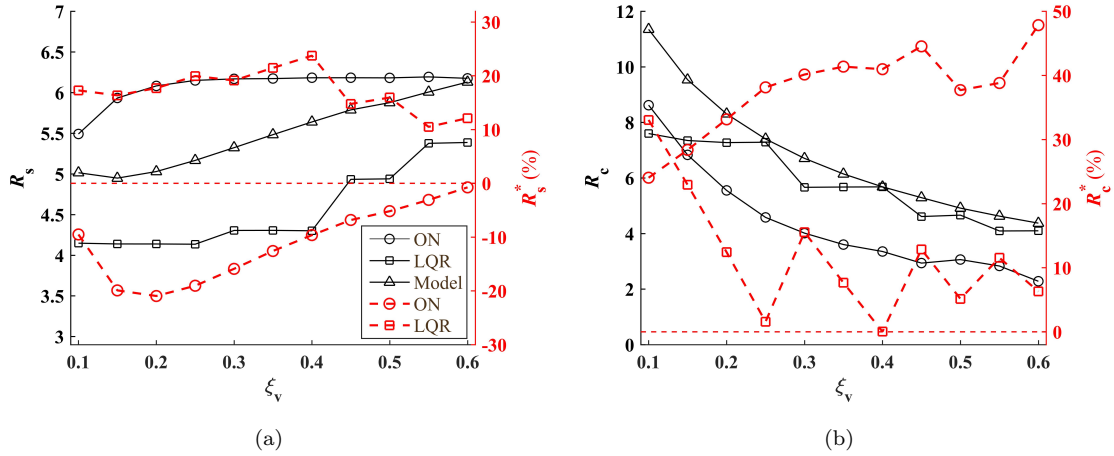


Figure 18: Comparison of the non-dimensional design factors - 5-story building: (a) R_s ; and (b) R_c .

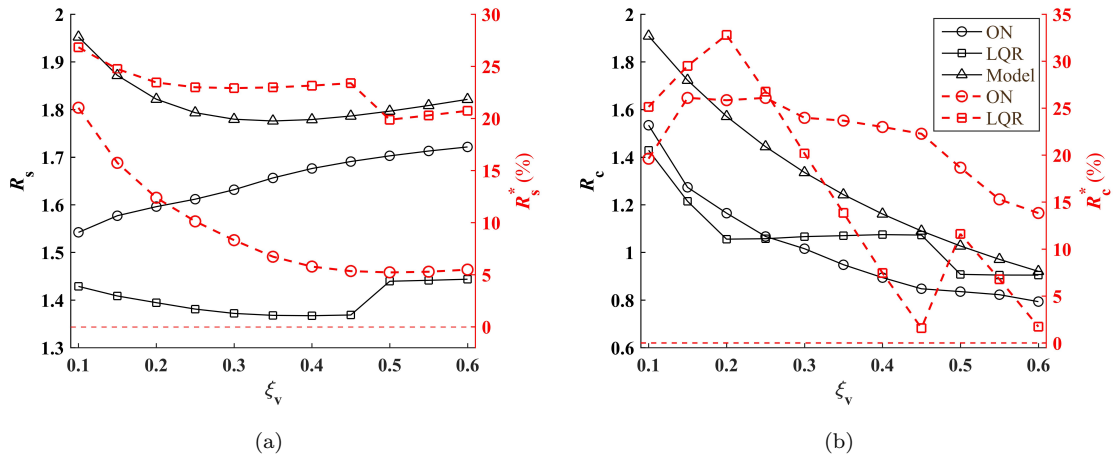


Figure 19: Comparison of the non-dimensional design factors - 20-story building: (a) R_s ; and (b) R_c .

429 **6. Conclusion**

430 A novel variable friction cladding connection (VFCC) has been previously proposed by the authors
 431 to enhance structural performance against multi-hazards and motion-based design methodology (MBD)
 432 developed to mitigate blast and wind-induced loads. This paper extended results to seismic application.

433 Analytical transfer functions for a structure-cladding system were derived. Specifically, two transfer
 434 functions representing the amplified structural displacement and the amplified structure-cladding relative
 435 displacement were obtained based on the assumption that the structure-cladding system can be reduced into
 436 a two degrees-of-freedom system. The quality of the assumption was verified through numerical simulations,

437 and results showed good agreement between the numerical and analytical solutions, but with increasing
438 disagreement for relatively high damping likely due to ignored nonlinearities in the high friction damping
439 regime, such as the stick-slip phenomenon. After the quantification of the seismic hazards and establishment
440 of motion performance metrics, design parameters were selected iteratively based on the analytical transfer
441 function to satisfy motion criteria for the given seismic loads.

442 The MBD procedure was then verified and demonstrated on a short 5-story building and a tall 20-story
443 building. The VFCCs were simulated in each building with their designed dynamic parameters based on
444 the proposed MBD procedure. The performance of the semi-actively controlled cladding connection was
445 compared against that of a passive friction case and the uncontrolled building. Simulation results show
446 that the semi-actively controlled VFCC significantly reduced structural responses compared against both
447 the passive-on and uncontrolled cases. It was also found that the passive-on mode used in the design of
448 the VFCC underestimated the maximum inter-story drift ratio. This was attributed to various analytical
449 assumptions made in order to facilitate a quick selection of the cladding connection parameters at design
450 phase. Nevertheless, analytical design solutions always overestimated the maximum structural responses
451 when the VFCC was used semi-actively, as intended, therefore providing a conservative design. The VFCC
452 was shown to be a promising device at mitigating seismic loads.

453 Appendix I Closed-form expression for the integral of rational functions

Consider an integral of the following form

$$J = \int_{-\infty}^{+\infty} \frac{g_n(\lambda)d\lambda}{h_n(\lambda)h_n(-\lambda)} \quad (57)$$

with

$$g_n(\lambda) = b_0\lambda^{2n-2} + b_1\lambda^{2n-4} + \dots + b_{n-1} \quad (58)$$

and

$$h_n(x) = a_0\lambda^n + a_1\lambda^{n-1} + \dots + a_n \quad (59)$$

454 its analytical solution follows [79]

$$J = \frac{j\pi Q_n}{a_0 V_n} \quad (60)$$

455 where j is the imaginary unit, and V_n and Q_n are the determinants of the following matrices

$$V_n = \begin{vmatrix} a_1 & a_3 & a_5 & \cdots & 0 \\ a_0 & a_2 & a_4 & \cdots & 0 \\ 0 & a_1 & a_3 & \cdots & 0 \\ \vdots & \vdots & \vdots & \ddots & \vdots \\ 0 & 0 & 0 & \cdots & a_n \end{vmatrix} \quad \text{and} \quad Q_n = \begin{vmatrix} b_0 & b_1 & b_2 & \cdots & b_{n-1} \\ a_0 & a_2 & a_4 & \cdots & 0 \\ 0 & a_1 & a_3 & \cdots & 0 \\ \vdots & \vdots & \vdots & \ddots & \vdots \\ 0 & 0 & 0 & \cdots & a_n \end{vmatrix} \quad (61)$$

456 Applying the above integral formula to solve J_s in Eq. 33 yields the corresponding function parameters
 457 in J_s

$$g_4(\lambda) = b_{s0}\lambda^6 + b_{s1}\lambda^4 + b_{s2}\lambda^2 + b_{s3}$$

$$h_4(\lambda) = a_{s0}\lambda^4 + a_{s1}\lambda^3 + a_{s2}\lambda^2 + a_{s3}\lambda + a_{s4}$$

458 and analytical solution

$$J_s = \pi j \frac{-a_{s3}a_{s4}b_{s1} + a_{s1}a_{s4}b_{s2} + b_{s3}(a_{s0}a_{s3} - a_{s1}a_{s2})}{a_{s4}(a_{s0}a_{s3}^2 + a_{s1}^2a_{s4} - a_{s1}a_{s2}a_{s3})} \quad (62)$$

459 where the constants $a_{s0} = 1$, $a_{s1} = -2j [\xi_c f (1 + \mu\Gamma_2) + \xi_s]$, $a_{s2} = -[(1 + \mu\Gamma_2) f^2 + 4\xi_s \xi_c f + 1]$, $a_{s3} =$
 460 $2j f (\xi_c + \xi_s f)$, $a_{s4} = f^2$, $b_{s0} = 0$, $b_{s1} = \Gamma_m^2$, $b_{s2} = [2\xi_c f (\mu\Gamma + \Gamma_m)]^2 - 2(\mu\Gamma + \Gamma_m)\Gamma_m f^2$, and $b_{s3} =$
 461 $(\mu\Gamma + \Gamma_m)^2 f^4$.

462 Similarly, the functions associated with J_{ci} in Eq.37 are written

$$g_6(\lambda) = b_{c0}\lambda^{10} + b_{c1}\lambda^8 + b_{c2}\lambda^6 + b_{c3}\lambda^4 + b_{c4}\lambda^2 + b_{c5}$$

$$h_6(\lambda) = a_{c0}\lambda^6 + a_{c1}\lambda^5 + a_{c2}\lambda^4 + a_{c3}\lambda^3 + a_{c4}\lambda^2 + a_{c5}\lambda + a_{c6}$$

463 where the constants $a_{c0} = -1$, $a_{c1} = -2j [\xi_c f (2 + \mu\Gamma_2) + \xi_s]$, $a_{c2} = [4\xi_c^2 (1 + \mu\Gamma_2) + \mu\Gamma_2 + 2] f^2 + 8\xi_c \xi_s f +$
 464 1 , $a_{c3} = 4j f [\xi_c (1 + \mu\Gamma_2) f^2 + \xi_s (2\xi_c^2 + 1) f + \xi_c]$, $a_{c4} = -f^2 [(1 + \mu\Gamma_2) f^2 + 8\xi_c \xi_s f + 4\xi_c^2 + 2]$, $a_{c5} =$
 465 $-2j f^3 (\xi_s f + 2\xi_c)$, and $a_{c6} = f^4$; and $b_{c0} = 0$, $b_{c1} = \Lambda_4^2$, $b_{c2} = 2\Lambda_2\Lambda_4 + \Lambda_3^2$, $b_{c3} = 2\Lambda_0\Lambda_4 + 2\Lambda_1\Lambda_3 + \Lambda_2^2$, $b_{c4} =$
 466 $2\Lambda_0\Lambda_2 + \Lambda_1^2$, and $b_{c5} = \Lambda_0^2$ with $\Lambda_0 = f^2$, $\Lambda_1 = 2f (\xi_c + \xi_s f)$, $\Lambda_2 = [\alpha_i (\mu\Gamma_1 + \Gamma_m) - \mu\Gamma_2 - 1] f^2 - 4\xi_c \xi_s f - 1$,
 467 $\Lambda_3 = 2j [\alpha_i \xi_c (\mu\Gamma_1 + \Gamma_m) f - \xi_c (1 + \mu\Gamma_2) f - \xi_s]$, and $\Lambda_4 = 1 - \alpha_i \Gamma_m$. Substituting these constants into Eq.
 468 61, the analytical solution for J_{ci} can be expressed in terms of the determinants of matrices V_n and Q_n using
 469 Eq. 60.

470 Acknowledgments

471 This material is based upon the work supported by the National Science Foundation under Grant No.
 472 1463252 and No. 1463497. Their support is gratefully acknowledged. Any opinions, findings, and conclusions
 473 or recommendations expressed in this material are those of the author(s) and do not necessarily reflect the
 474 views of the National Science Foundation.

475 References

- 476 [1] J. Connor, S. Laflamme, Structural motion engineering, Springer, 2014.
- 477 [2] L. Moreschi, M. Singh, Design of yielding metallic and friction dampers for optimal seismic performance,
 478 Earthquake engineering & structural dynamics 32 (8) (2003) 1291–1311.

- 479 [3] R. Vargas, M. Bruneau, Effect of supplemental viscous damping on the seismic response of structural
480 systems with metallic dampers, *Journal of Structural Engineering* 133 (10) (2007) 1434–1444.
- 481 [4] W. L. Qu, Z. H. Chen, Y.-L. Xu, Dynamic analysis of wind-excited truss tower with friction dampers,
482 *Computers & structures* 79 (32) (2001) 2817–2831.
- 483 [5] I. H. Mualla, B. Belev, Performance of steel frames with a new friction damper device under earthquake
484 excitation, *Engineering Structures* 24 (3) (2002) 365–371.
- 485 [6] K.-W. Min, J. Kim, S.-H. Lee, Vibration tests of 5-storey steel frame with viscoelastic dampers, *Engi-
486 neering Structures* 26 (6) (2004) 831–839.
- 487 [7] J.-H. Park, J. Kim, K.-W. Min, Optimal design of added viscoelastic dampers and supporting braces,
488 *Earthquake engineering & structural dynamics* 33 (4) (2004) 465–484.
- 489 [8] K. K. Wong, Seismic energy analysis of structures with nonlinear fluid viscous dampers algorithm and
490 numerical verification, *The Structural Design of Tall and Special Buildings* 20 (4) (2011) 482–496.
- 491 [9] C.-Y. Seo, T. L. Karavasilis, J. M. Ricles, R. Sause, Seismic performance and probabilistic collapse resis-
492 tance assessment of steel moment resisting frames with fluid viscous dampers, *Earthquake Engineering
493 & Structural Dynamics* 43 (14) (2014) 2135–2154.
- 494 [10] C.-C. Lin, J.-M. Ueng, T.-C. Huang, Seismic response reduction of irregular buildings using passive
495 tuned mass dampers, *Engineering Structures* 22 (5) (2000) 513–524.
- 496 [11] C.-C. Lin, C.-L. Chen, J.-F. Wang, Vibration control of structures with initially accelerated passive
497 tuned mass dampers under near-fault earthquake excitation, *Computer-Aided Civil and Infrastructure
498 Engineering* 25 (1) (2010) 69–75.
- 499 [12] M. Symans, F. Charney, A. Whittaker, M. Constantinou, C. Kircher, M. Johnson, R. McNamara,
500 Energy dissipation systems for seismic applications: current practice and recent developments, *Journal
501 of structural engineering* 134 (1) (2008) 3–21.
- 502 [13] G. Ma, Z. Ye, Energy absorption of double-layer foam cladding for blast alleviation, *International
503 Journal of Impact Engineering* 34 (2) (2007) 329–347. doi:10.1016/j.ijimpeng.2005.07.012.
504 URL <https://doi.org/10.1016/j.ijimpeng.2005.07.012>
- 505 [14] C. Wu, H. Sheikh, A finite element modelling to investigate the mitigation of blast effects on reinforced
506 concrete panel using foam cladding, *International journal of impact engineering* 55 (2013) 24–33.
- 507 [15] M. Theobald, G. Nurick, Experimental and numerical analysis of tube-core claddings under blast loads,
508 *International Journal of Impact Engineering* 37 (3) (2010) 333–348. doi:10.1016/j.ijimpeng.2009.

- 509 10.003.
510 URL <https://doi.org/10.1016/j.ijimpeng.2009.10.003>
- 511 [16] W. Van Paepegem, S. Palanivelu, J. Degrieck, J. Vantomme, B. Reymen, D. Kakogiannis, D. Van Hemel-
512 rijck, J. Wastiels, Blast performance of a sacrificial cladding with composite tubes for protection of civil
513 engineering structures, *Composites Part B: Engineering* 65 (2014) 131–146.
- 514 [17] S. C. K. Yuen, G. Nurick, M. Theobald, G. Langdon, Sandwich panels subjected to blast loading, in:
515 *Dynamic failure of materials and structures*, Springer, 2009, pp. 297–325.
- 516 [18] R. Alberdi, J. Przywara, K. Khandelwal, Performance evaluation of sandwich panel systems for blast
517 mitigation, *Engineering Structures* 56 (2013) 2119–2130. doi:10.1016/j.engstruct.2013.08.021.
518 URL <https://doi.org/10.1016/j.engstruct.2013.08.021>
- 519 [19] G. Langdon, G. Schleyer, Deformation and failure of profiled stainless steel blast wall panels. part III:
520 finite element simulations and overall summary, *International Journal of Impact Engineering* 32 (6)
521 (2006) 988–1012. doi:10.1016/j.ijimpeng.2004.08.002.
522 URL <https://doi.org/10.1016/j.ijimpeng.2004.08.002>
- 523 [20] A. Hanssen, L. Enstock, M. Langseth, Close-range blast loading of aluminium foam panels, *International*
524 *Journal of Impact Engineering* 27 (6) (2002) 593–618.
- 525 [21] W. Chen, H. Hao, Numerical study of blast-resistant sandwich panels with rotational friction dampers,
526 *International Journal of Structural Stability and Dynamics* 13 (06) (2013) 1350014. doi:10.1142/
527 s0219455413500144.
528 URL <https://doi.org/10.1142/s0219455413500144>
- 529 [22] W. S. Chen, H. Hao, Preliminary study of sandwich panel with rotational friction hinge device against
530 blast loadings, *Key Engineering Materials* 535-536 (2013) 530–533. doi:10.4028/www.scientific.
531 net/kem.535-536.530.
532 URL <https://doi.org/10.4028/www.scientific.net/kem.535-536.530>
- 533 [23] C. Amadio, C. Bedon, Viscoelastic spider connectors for the mitigation of cable-supported façades
534 subjected to air blast loading, *Engineering Structures* 42 (2012) 190–200. doi:10.1016/j.engstruct.
535 2012.04.023.
536 URL <https://doi.org/10.1016/j.engstruct.2012.04.023>
- 537 [24] Y. Wang, J. R. Liew, S. C. Lee, X. Zhai, W. Wang, Crushing of a novel energy absorption connector
538 with curved plate and aluminum foam as energy absorber, *Thin-Walled Structures* 111 (2017) 145–154.

539 doi:10.1016/j.tws.2016.11.019.

540 URL <https://doi.org/10.1016/j.tws.2016.11.019>

541 [25] B. Goodno, J. Craig, L. El-Gazairly, C. Hsu, Use of advanced cladding systems for passive control of
542 building response in earthquakes, in: Proceedings, 10th World Conference on Earthquake Engineering,
543 July, 1992, pp. 19–24.

544 [26] A. Baird, R. Diaferia, A. Palermo, S. Pampanin, Parametric investigation of seismic interaction between
545 precast concrete cladding systems and moment resisting frames, in: Structures Congress 2011, American
546 Society of Civil Engineers, 2011. doi:10.1061/41171(401)114.

547 URL [https://doi.org/10.1061/41171\(401\)114](https://doi.org/10.1061/41171(401)114)

548 [27] A. Azad, B. Samali, T. Ngo, C. Nguyen, Dynamic behaviour of flexible facade systems in tall buildings
549 subjected to wind loads, From Materials to Structures: Advancement through Innovation (2013) 431–
550 435.

551 [28] A. Azad, T. Ngo, B. Samali, Control of wind-induced motion of tall buildings using smart facade
552 systems, Electronic Journal of Structural Engineering 14 (2015) 33–40.

553 [29] F. Biondini, B. Dal Lago, G. Toniolo, Experimental and numerical assessment of dissipative connections
554 for precast structures with cladding panels, in: 2nd European conference on earthquake engineering and
555 seismology (ECEES), Istanbul, Turkey, Vol. 2168, 2014, pp. 25–29.

556 [30] L. Ferrara, R. Felicetti, G. Toniolo, C. Zenti, Friction dissipative devices for cladding panels in precast
557 buildings. an experimental investigation, European Journal of Environmental and Civil engineering
558 15 (9) (2011) 1319–1338. doi:10.3166/ejece.15.1319–1338.

559 URL <https://doi.org/10.3166/ejece.15.1319–1338>

560 [31] H. Maneetes, A. Memari, Introduction of an innovative cladding panel system for multi-story buildings,
561 Buildings 4 (3) (2014) 418–436. doi:10.3390/buildings4030418.

562 URL <https://doi.org/10.3390/buildings4030418>

563 [32] B. Dal Lago, F. Biondini, G. Toniolo, Experimental investigation on steel w-shaped folded plate dissi-
564 pative connectors for horizontal precast concrete cladding panels, Journal of Earthquake Engineering
565 22 (5) (2018) 778–800.

566 [33] P. Abtahi, B. Samali, Evaluation of in-plane and out-of-plane movement of façade panels to reduce
567 structure response during earthquake excitation, in: 23rd Australasian Conference on the Mechanics of
568 Structures and Materials (ACMSM23), Lismore, Australia, Vol. 2, Southern Cross University, 2014, pp.
569 967–972.

- 570 [34] T. S. Fu, R. Zhang, Integrating double-skin façades and mass dampers for structural safety and energy
571 efficiency, *Journal of Architectural Engineering* 22 (4) (2016) 04016014.
- 572 [35] G. Pipitone, G. Barone, A. Palmeri, Optimal design of double-skin façades as vibration absorbers,
573 *Structural Control and Health Monitoring* 25 (2) (2018) e2086.
- 574 [36] J. N. Yang, A. K. Agrawal, Semi-active hybrid control systems for nonlinear buildings against near-field
575 earthquakes, *Engineering structures* 24 (3) (2002) 271–280.
- 576 [37] L. Cao, S. Laflamme, D. Taylor, J. Ricles, Simulations of a variable friction device for multihazard
577 mitigation, *Journal of Structural Engineering* 142 (12) (2016) H4016001. doi:10.1061/(asce)st.
578 1943-541x.0001580.
579 URL [https://doi.org/10.1061/\(asce\)st.1943-541x.0001580](https://doi.org/10.1061/(asce)st.1943-541x.0001580)
- 580 [38] F. Ubertini, Active feedback control for cable vibrations, *Smart Structures and Systems* 4 (4) (2008)
581 407–428.
- 582 [39] A. L. Materazzi, F. Ubertini, Robust structural control with system constraints, *Structural Control and*
583 *Health Monitoring* 19 (3) (2012) 472–490.
- 584 [40] I. Venanzi, F. Ubertini, A. L. Materazzi, Optimal design of an array of active tuned mass dampers for
585 wind-exposed high-rise buildings, *Structural Control and Health Monitoring* 20 (6) (2013) 903–917.
- 586 [41] L. Cao, A. Downey, S. Laflamme, D. Taylor, J. Ricles, Variable friction device for structural control based
587 on duo-servo vehicle brake: Modeling and experimental validation, *Journal of Sound and Vibration* 348
588 (2015) 41–56. doi:10.1016/j.jsv.2015.03.011.
589 URL <https://doi.org/10.1016/j.jsv.2015.03.011>
- 590 [42] A. Downey, L. Cao, S. Laflamme, D. Taylor, J. Ricles, High capacity variable friction damper based on
591 band brake technology, *Engineering Structures* 113 (2016) 287–298.
- 592 [43] M. Amjadian, A. K. Agrawal, Vibration control using a variable coil-based friction damper, in: *Active*
593 *and Passive Smart Structures and Integrated Systems 2017*, Vol. 10164, International Society for Optics
594 and Photonics, 2017, p. 101642J.
- 595 [44] J. Love, M. Tait, H. Toopchi-Nezhad, A hybrid structural control system using a tuned liquid damper
596 to reduce the wind induced motion of a base isolated structure, *Engineering Structures* 33 (3) (2011)
597 738–746.
- 598 [45] Y.-H. Shin, S.-J. Moon, J.-M. Kim, H.-Y. Cho, J.-Y. Choi, H.-W. Cho, Design considerations of linear
599 electromagnetic actuator for hybrid-type active mount damper, *IEEE Transactions on Magnetics* 49 (7)
600 (2013) 4080–4083.

- 601 [46] J. Høgsberg, M. L. Brodersen, Hybrid viscous damper with filtered integral force feedback control,
602 Journal of Vibration and Control 22 (6) (2016) 1645–1656.
- 603 [47] B. Spencer Jr, S. Nagarajaiah, State of the art of structural control, Journal of structural engineering
604 129 (7) (2003) 845–856.
- 605 [48] L. Cao, S. Laflamme, Real-time variable multidelay controller for multihazard mitigation, Journal of
606 Engineering Mechanics 144 (2) (2018) 04017174. doi:10.1061/(asce)em.1943-7889.0001406.
- 607 [49] S. Narasimhan, S. Nagarajaiah, Smart base isolated buildings with variable friction systems: H_∞
608 controller and saivf device, Earthquake engineering & structural dynamics 35 (8) (2006) 921–942.
- 609 [50] Y. Kawamoto, Y. Suda, H. Inoue, T. Kondo, Electro-mechanical suspension system considering energy
610 consumption and vehicle manoeuvre, Vehicle System Dynamics 46 (S1) (2008) 1053–1063.
- 611 [51] M. Lorenz, B. Heimann, V. Härtel, A novel engine mount with semi-active dry friction damping, Shock
612 and Vibration 13 (4-5) (2006) 559–571. doi:10.1155/2006/263251.
613 URL <https://doi.org/10.1155/2006/263251>
- 614 [52] H. Dai, Z. Liu, W. Wang, Structural passive control on electromagnetic friction energy dissipation
615 device, Thin-Walled Structures 58 (2012) 1–8. doi:10.1016/j.tws.2012.03.017.
616 URL <https://doi.org/10.1016/j.tws.2012.03.017>
- 617 [53] M. A. Karkoub, M. Zribi, Active/semi-active suspension control using magnetorheological actuators,
618 International journal of systems science 37 (1) (2006) 35–44.
- 619 [54] S. Bharti, S. Dumne, M. Shrimali, Seismic response analysis of adjacent buildings connected with mr
620 dampers, Engineering Structures 32 (8) (2010) 2122–2133.
- 621 [55] M. Mirtaheeri, A. P. Zandi, S. S. Samadi, H. R. Samani, Numerical and experimental study of hysteretic
622 behavior of cylindrical friction dampers, Engineering Structures 33 (12) (2011) 3647–3656.
- 623 [56] D. Zhao, H. Li, Shaking table tests and analyses of semi-active fuzzy control for structural seismic
624 reduction with a piezoelectric variable-friction damper, Smart Materials and Structures 19 (10) (2010)
625 105031. doi:10.1088/0964-1726/19/10/105031.
626 URL <https://doi.org/10.1088/0964-1726/19/10/105031>
- 627 [57] J. Pardo-Varela, J. Llera, A semi-active piezoelectric friction damper, Earthquake Engineering & Struc-
628 tural Dynamics 44 (3) (2015) 333–354.
- 629 [58] Y. Gong, L. Cao, S. Laflamme, S. Quiel, J. Ricles, D. Taylor, Characterization of a novel variable
630 friction connection for semiactive cladding system, Structural Control and Health Monitoring 25 (6)

- 631 (2018) e2157. doi:10.1002/stc.2157.
632 URL <https://doi.org/10.1002/stc.2157>
- 633 [59] L. Cao, S. Lu, S. Laflamme, S. Quiel, J. Ricles, D. Taylor, Performance-based design procedure of a novel
634 friction-based cladding connection for blast mitigation, *International Journal of Impact Engineering* 117
635 (2018) 48–62. doi:10.1016/j.ijimpeng.2018.03.003.
636 URL <https://doi.org/10.1016/j.ijimpeng.2018.03.003>
- 637 [60] Y. Gong, L. Cao, S. Laflamme, J. Ricles, S. Quiel, D. Taylor, Motion-based design approach for a novel
638 variable friction cladding connection used in wind hazard mitigation, *Engineering Structures* 181 (2019)
639 397–412. doi:10.1016/j.engstruct.2018.12.033.
- 640 [61] A. K. Chopra, *Dynamics of structures: theory and applications to earthquake engineering*. 2007, Google
641 Scholar (2007) 470–472.
- 642 [62] J. Scruggs, W. Iwan, Control of a civil structure using an electric machine with semiactive capability,
643 *Journal of Structural Engineering* 129 (7) (2003) 951–959.
- 644 [63] G. J. Hiemenz, W. Hu, N. M. Wereley, Semi-active magnetorheological helicopter crew seat suspension
645 for vibration isolation, *Journal of Aircraft* 45 (3) (2008) 945–953.
- 646 [64] A. Giaralis, P. D. Spanos, Effective linear damping and stiffness coefficients of nonlinear systems for
647 design spectrum based analysis, *Soil Dynamics and Earthquake Engineering* 30 (9) (2010) 798–810.
- 648 [65] C. A. Martínez, O. Curadelli, M. E. Compagnoni, Optimal design of passive viscous damping systems
649 for buildings under seismic excitation, *Journal of Constructional Steel Research* 90 (2013) 253–264.
- 650 [66] E. H. Vanmarcke, Structural response to earthquakes, in: *Developments in Geotechnical Engineering*,
651 Vol. 15, Elsevier, 1976, pp. 287–337.
- 652 [67] P. Cacciola, P. Colajanni, G. Muscolino, Combination of modal responses consistent with seismic input
653 representation, *Journal of Structural Engineering* 130 (1) (2004) 47–55.
- 654 [68] ASCE, *Minimum Design Loads for Buildings and Other Structures*, American Society of Civil Engineer-
655 ing, Reston, VA, asce/sei 7-10 edition., 2010.
- 656 [69] G. Calvi, M. Priestley, M. Kowalsky, Displacement-based seismic design of structures, in: *3rd National*
657 *Conference on Earthquake Engineering and Engineering Seismology*, Citeseer, 2008.
- 658 [70] A. Ghobarah, Performance-based design in earthquake engineering: state of development, *Engineering*
659 *structures* 23 (8) (2001) 878–884.

- 660 [71] Y.-J. Cha, A. K. Agrawal, B. M. Phillips, B. F. Spencer Jr, Direct performance-based design with 200
661 kn mr dampers using multi-objective cost effective optimization for steel mrfs, *Engineering Structures*
662 71 (2014) 60–72.
- 663 [72] Q. Xue, C.-C. Chen, Performance-based seismic design of structures: a direct displacement-based ap-
664 proach, *Engineering Structures* 25 (14) (2003) 1803–1813.
- 665 [73] A. Ghobarah, On drift limits associated with different damage levels, in: *Performance-Based Seismic*
666 *Design Concepts and Implementation: Proceedings of the International Workshop, Bled, Slovenia,*
667 *Vol. 28, 2004, pp. 321–332.*
- 668 [74] J.-P. Pinelli, J. I. Craig, B. J. Goodno, Energy-based seismic design of ductile cladding systems, *Journal*
669 *of Structural Engineering* 121 (3) (1995) 567–578.
- 670 [75] A. Der Kiureghian, Structural response to stationary excitation, *Journal of the Engineering Mechanics*
671 *Division* 106 (6) (1980) 1195–1213.
- 672 [76] Q. Li, J. Wu, S. Liang, Y. Xiao, C. Wong, Full-scale measurements and numerical evaluation of wind-
673 induced vibration of a 63-story reinforced concrete tall building, *Engineering structures* 26 (12) (2004)
674 1779–1794.
- 675 [77] K.-W. Min, J.-Y. Seong, J. Kim, Simple design procedure of a friction damper for reducing seismic
676 responses of a single-story structure, *Engineering Structures* 32 (11) (2010) 3539–3547. doi:10.1016/
677 j.engstruct.2010.07.022.
678 URL <https://doi.org/10.1016/j.engstruct.2010.07.022>
- 679 [78] S. H. Crandall, W. D. Mark, *Random vibration in mechanical systems*, Academic Press, 2014.
- 680 [79] I. S. Gradshteyn, I. M. Ryzhik, *Table of integrals, series, and products*, Academic press, 2014.
- 681 [80] C. A. Maniatakis, I. N. Psycharis, C. C. Spyarakos, Effect of higher modes on the seismic response and
682 design of moment-resisting rc frame structures, *Engineering Structures* 56 (2013) 417–430.
- 683 [81] N. Kurata, T. Kobori, M. Takahashi, N. Niwa, H. Midorikawa, Actual seismic response controlled
684 building with semi-active damper system, *Earthquake engineering & structural dynamics* 28 (11) (1999)
685 1427–1447.
- 686 [82] Y. Ohtori, R. Christenson, B. Spencer Jr, S. Dyke, Benchmark control problems for seismically excited
687 nonlinear buildings, *Journal of Engineering Mechanics* 130 (4) (2004) 366–385.
- 688 [83] E. Pantoli, T. C. Hutchinson, Experimental and analytical study of the dynamic characteristics of
689 architectural precast concrete cladding, in: *Improving the Seismic Performance of Existing Buildings and*

- 690 Other Structures 2015, American Society of Civil Engineers, 2015. doi:10.1061/9780784479728.046.
691 URL <https://doi.org/10.1061/9780784479728.046>
- 692 [84] M. G. Soto, H. Adeli, Vibration control of smart base-isolated irregular buildings using neural dynamic
693 optimization model and replicator dynamics, Engineering Structures 156 (2018) 322–336. doi:10.1016/
694 j.engstruct.2017.09.037.
- 695 [85] L. Cao, S. Laflamme, J. Hong, J. Dodson, Input space dependent controller for civil structures exposed
696 to multi-hazard excitations, Engineering Structures 166 (2018) 286–301. doi:10.1016/j.engstruct.
697 2018.03.083.
- 698 [86] T. S. Fu, E. A. Johnson, Distributed mass damper system for integrating structural and environmental
699 controls in buildings, Journal of Engineering Mechanics 137 (3) (2011) 205–213. doi:10.1061/(asce)
700 em.1943-7889.0000211.
701 URL [https://doi.org/10.1061/\(asce\)em.1943-7889.0000211](https://doi.org/10.1061/(asce)em.1943-7889.0000211)
- 702 [87] Pacific Earthquake Engineering Research Center (PEER), 2011. PEER Ground Motion Database, avail-
703 able at <http://ngawest2.berkeley.edu/>.
- 704 [88] M. Liu, S. A. Burns, Y. Wen, Multiobjective optimization for performance-based seismic design of steel
705 moment frame structures, Earthquake Engineering & Structural Dynamics 34 (3) (2005) 289–306.